

# Energetic Constraints on the Pattern of Changes to the Hydrological Cycle under Global Warming

DAVID B. BONAN,<sup>a</sup> NICHOLAS SILER,<sup>b</sup> GERARD H. ROE,<sup>c</sup> AND KYLE C. ARMOUR<sup>c</sup>

<sup>a</sup> *California Institute of Technology, Pasadena, California*

<sup>b</sup> *Oregon State University, Corvallis, Oregon*

<sup>c</sup> *University of Washington, Seattle, Washington*

(Manuscript received 10 May 2022, in final form 20 January 2023)

**ABSTRACT:** The response of zonal-mean precipitation minus evaporation ( $P - E$ ) to global warming is investigated using a moist energy balance model (MEBM) with a simple Hadley cell parameterization. The MEBM accurately emulates zonal-mean  $P - E$  change simulated by a suite of global climate models (GCMs) under greenhouse gas forcing. The MEBM also accounts for most of the intermodel differences in GCM  $P - E$  change and better emulates GCM  $P - E$  change when compared to the “wet-gets-wetter, dry-gets-drier” thermodynamic mechanism. The intermodel spread in  $P - E$  change is attributed to intermodel differences in radiative feedbacks, which account for 60%–70% of the intermodel variance, with smaller contributions from radiative forcing and ocean heat uptake. Isolating the intermodel spread of feedbacks to specific regions shows that tropical feedbacks are the primary source of intermodel spread in zonal-mean  $P - E$  change. The ability of the MEBM to emulate GCM  $P - E$  change is further investigated using idealized feedback patterns. A less negative and narrowly peaked feedback pattern near the equator results in more atmospheric heating, which strengthens the Hadley cell circulation in the deep tropics through an enhanced poleward heat flux. This pattern also increases gross moist stability, which weakens the subtropical Hadley cell circulation. These two processes in unison increase  $P - E$  in the deep tropics, decrease  $P - E$  in the subtropics, and narrow the intertropical convergence zone. Additionally, a feedback pattern that produces polar-amplified warming partially reduces the poleward moisture flux by weakening the meridional temperature gradient. It is shown that changes to the Hadley cell circulation and the poleward moisture flux are crucial for understanding the pattern of GCM  $P - E$  change under warming.

**SIGNIFICANCE STATEMENT:** Changes to the hydrological cycle over the twenty-first century are predicted to impact ecosystems and socioeconomic activities throughout the world. While it is broadly expected that dry regions will get drier and wet regions will get wetter, the magnitude and spatial structure of these changes remains uncertain. In this study, we use an idealized climate model, which assumes how energy is transported in the atmosphere, to understand the processes setting the pattern of precipitation and evaporation under global warming. We first use the idealized climate model to explain why comprehensive climate models predict different changes to precipitation and evaporation across a range of latitudes. We show this arises primarily from climate feedbacks, which act to amplify or dampen the amount of warming. Ocean heat uptake and radiative forcing play secondary roles but can account for a significant amount of the uncertainty in regions where ocean circulation influences the rate of warming. We further show that uncertainty in tropical feedbacks (mainly from clouds) affects changes to the hydrological cycle across a range of latitudes. We then show how the pattern of climate feedbacks affects how the patterns of precipitation and evaporation respond to climate change through a set of idealized experiments. These results show how the pattern of climate feedbacks impacts tropical hydrological changes by affecting the strength of the Hadley circulation and polar hydrological changes by affecting the transport of moisture to the high latitudes.

**KEYWORDS:** Atmospheric circulation; Energy transport; Feedback; Precipitation; Climate change; Climate models

## 1. Introduction

The hydrological cycle, which describes the continuous movement of water on Earth, is a key component of the climate system. A fundamental measure of the hydrological cycle is the net water flux into the surface, which is equal to the difference between precipitation and evaporation ( $P - E$ ). The magnitude and spatial pattern of  $P - E$  affects the formation of water masses in the ocean (e.g., Schmitt et al. 1989; Large and Nurser 2001; Abernathy et al. 2016; Groeskamp et al. 2019), the salinity and stratification of the ocean’s mixed

layer (e.g., de Boyer Montégut et al. 2007), and the amount of runoff or availability of water over the land (e.g., Dai and Trenberth 2002; Field and Barros 2014). The pattern of  $P - E$  can also modulate transient climate change through changes in upper-ocean salinity, which impacts the degree of ocean heat uptake by changing the vertical stratification of the ocean (e.g., Liu et al. 2021). The magnitude and spatial pattern of  $P - E$  has been dramatically different in past climate states (e.g., Winguth et al. 2010; Boos 2012; Carmichael et al. 2016; Burls and Fedorov 2017) and is predicted to change substantially over the next century (e.g., Mitchell et al. 1987; Chou and Neelin 2004; Held and Soden 2006; Byrne and O’Gorman 2015).

In response to increased greenhouse gas concentrations, state-of-the-art global climate models (GCMs) consistently

*Corresponding author:* David B. Bonan, dbonan@caltech.edu

DOI: 10.1175/JCLI-D-22-0337.1

© 2023 American Meteorological Society. For information regarding reuse of this content and general copyright information, consult the [AMS Copyright Policy](#) ([www.ametsoc.org/PUBSReuseLicenses](http://www.ametsoc.org/PUBSReuseLicenses)).

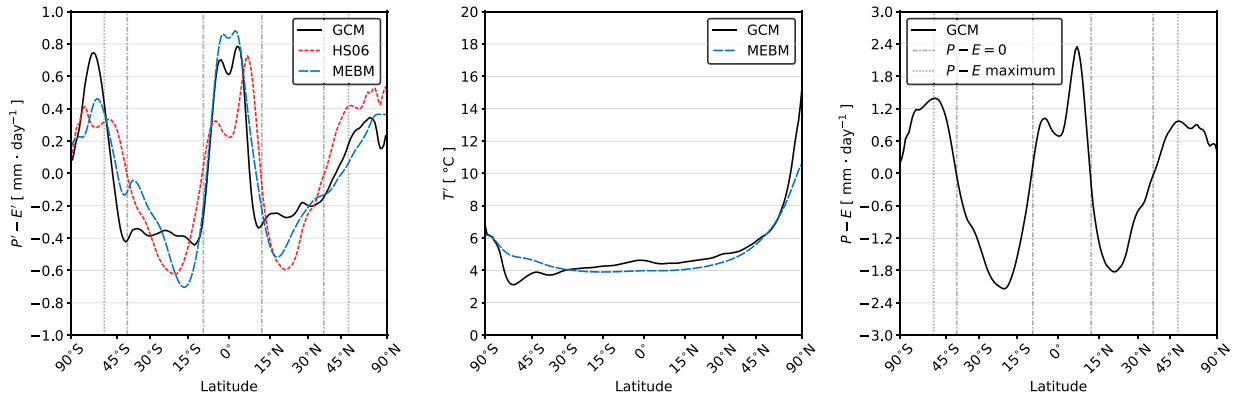


FIG. 1. Response of the hydrological cycle to global warming. (a) The multimodel mean change in zonal-mean precipitation minus evaporation ( $P' - E'$ ) from 20 CMIP5 simulations 126–150 years after an abrupt quadrupling of  $\text{CO}_2$  relative to the preindustrial average (black). The HS06 approximation (red dashed line) is calculated from Eq. (4) and found by applying the multimodel zonal-mean change in near-surface air temperature from the abrupt quadrupling of  $\text{CO}_2$  [black line in (b)] and the multimodel mean  $P - E$  climatology from the preindustrial-control simulations [in (c)] assuming  $\alpha = 7\% \text{ K}^{-1}$  globally. The blue line shows the MEBM  $P' - E'$  pattern (which is described in section 2). (b) The multimodel mean change in zonal-mean near-surface air temperature ( $T'$ ) of 20 CMIP5 GCMs and the MEBM (blue line) (see section 2). (c) The multimodel mean climatological zonal-mean precipitation minus evaporation ( $P - E$ ) of 20 CMIP5 GCMs. The gray dashed vertical lines in (a) and (c) represent the climatological  $P - E = 0$  in preindustrial control simulations, which corresponds to the subtropical regions; and the gray dotted vertical lines represent the climatological extratropical  $P - E$  maximum in preindustrial control simulations, which is a measure of the storm-track latitude.

predict enhanced tropical precipitation and reduced subtropical precipitation, particularly over the oceans. Held and Soden (2006) explained that this “wet-gets-wetter, dry-gets-drier” paradigm can be understood by assuming that the change in  $P - E$  with warming is due primarily to the change in moisture content of the atmosphere, with little contribution from changes in atmospheric circulations. A simple scaling for these changes can be derived from the fact that on climatological time scales,  $P - E$  is equal to the convergence of the mass-weighted, vertically integrated moisture flux  $F_L$ :

$$P - E = -\nabla \cdot F_L. \quad (1)$$

As discussed in Held and Soden (2006, hereafter HS06), the scaling arises by assuming the change in  $F_L$  is dominated by the change in lower-tropospheric specific humidity, with no changes in relative humidity and atmospheric circulation. These constraints mean that, as the atmosphere warms,  $F_L$  will increase at close to the Clausius–Clapeyron rate, implying that

$$F_L' \approx \alpha T' F_L, \quad (2)$$

where primes indicate the difference between the perturbed and control climates and

$$\alpha = \frac{L_v}{R_v T^2}, \quad (3)$$

is the Clausius–Clapeyron scaling factor, where  $L_v$  is the latent heat of vaporization ( $2.5 \times 10^6 \text{ J kg}^{-1}$ ),  $R_v$  is the gas constant of water vapor ( $461.5 \text{ J kg}^{-1} \text{ K}^{-1}$ ), and  $T$  is the near-surface air temperature. For typical atmospheric temperatures,  $\alpha$  ranges from around  $6\% \text{ K}^{-1}$  (when  $T = 30^{\circ}\text{C}$ ) to more than  $9\% \text{ K}^{-1}$  (when  $T = -30^{\circ}\text{C}$ ). If one assumes that gradients in  $\alpha$  and  $T'$

are relatively small, Eq. (2) suggests that the change in  $P - E$  under warming will also scale at the Clausius–Clapeyron rate, which results in

$$P' - E' \approx \alpha T' (P - E). \quad (4)$$

Equation (4) implies that spatially uniform warming will enhance the existing pattern of  $P - E$ : increasing  $P - E$  in the tropics and high latitudes and decreasing  $P - E$  in the subtropics (e.g., Chou and Neelin 2004; Emori and Brown 2005; HS06; Seager et al. 2010). Equation (4) also implies that the climatological boundaries of where  $P - E = 0$  will remain fixed.

HS06 found that Eq. (4) broadly captured the spatial structure of  $P' - E'$  as simulated by coupled GCMs under rising greenhouse gas concentrations. Figure 1a shows the multimodel mean, zonal-mean  $P - E$  change averaged over years 126–150 after an abrupt quadrupling of  $\text{CO}_2$  ( $4 \times \text{CO}_2$ ) for 20 GCMs participating in phase 5 of the Coupled Model Intercomparison Project (CMIP5). Under global warming, GCMs show increasing  $P - E$  in the tropics and high latitudes and decreasing  $P - E$  in the subtropics (see black line in Fig. 1a). The red dashed line shows the HS06 approximation from Eq. (4) using the multimodel mean patterns of  $T'$  (Fig. 1b) and  $P - E$  (Fig. 1c) from the same 20 GCMs, assuming that  $\alpha = 7\% \text{ K}^{-1}$  everywhere. Note, we use local values of  $T'$  in Eq. (4). While the approximation indeed captures the overall spatial pattern of  $P - E$  change in GCM simulations of global warming, there are a few aspects that are not captured. Namely, Eq. (4) predicts  $P - E$  changes that are too large in the Northern Hemisphere extratropics and in the subtropical regions of both hemispheres, and predicts  $P - E$  changes that are too small in the tropics and the Southern Hemisphere

extratropics. Furthermore, Eq. (4) does not capture other robust features of  $P - E$  changes as seen in GCMs, such as the poleward expansion of the subtropics (Lu et al. 2007; Kang and Lu 2012), a poleward shift of the  $P - E$  maximum associated with the midlatitude storm tracks (Lu et al. 2010; Chang et al. 2012; Mbengue and Schneider 2013, 2017, 2018), and a contraction of the intertropical convergence zone (ITCZ; Byrne and Schneider 2016b).

Some of the differences between the zonal-mean  $P - E$  change predicted by Eq. (4) and simulated by GCMs have been reconciled through additional terms that account for the spatial pattern of temperature change or changing atmospheric circulations. For instance, Boos (2012) showed that including the pattern of temperature change is necessary for understanding  $P - E$  change at the Last Glacial Maximum, where ice sheets greatly altered horizontal temperature gradients. Similarly, Byrne and O’Gorman (2015) showed that changes to the patterns of temperature and relative humidity are important when considering the response of  $P - E$  to warming over land, where warming is generally amplified and relative humidity generally decreases. Byrne and O’Gorman (2015) also noted that over traditionally dry land regions, such as deserts, may actually become wetter due to these additional terms. However, these modifications to the HS06 approximation are still fundamentally thermodynamic, and do not account for the potential impact of dynamical changes on the pattern of  $P - E$ . For example, the additional terms in Byrne and O’Gorman (2015) do not predict the increase in tropical  $P - E$  that GCMs suggest. Other studies have shown that changing atmospheric circulations play an important role in determining the degree of subtropical expansion and narrowing of the ITCZ (Seager et al. 2010; Seager and Vecchi 2010), as well as poleward shifts in the midlatitude storm tracks (Scheff and Frierson 2012).

More recently, Siler et al. (2018) simulated the change in zonal-mean  $P - E$  using a moist energy balance model (MEBM) and showed that this approach can capture most of these deviations from the “wet-gets-wetter, dry-gets-drier” paradigm. The MEBM assumes that atmospheric heat transport can be represented by downgradient transport of near-surface moist-static energy. However, Siler et al. (2018) included a simple Hadley cell parameterization in the MEBM, which transports latent energy upgradient in the tropics, and showed that the MEBM accurately emulates  $P - E$  change as simulated by coupled GCMs under global warming and better emulates these changes when compared to the HS06 approximation (see blue dashed line in Fig. 1a). In particular, the MEBM correctly simulates the larger increase in  $P - E$  in the deep tropics and more muted  $P - E$  changes in the Northern Hemisphere extratropics (Fig. 1a). The MEBM also predicts the GCM expansion of the subtropics both equatorward and poleward, which can be seen in Fig. 1a as regions where  $P' - E' < 0$  extend across the dash-dot vertical lines (i.e.,  $P - E = 0$  in the climatology). Likewise, the dotted vertical lines in Fig. 1a denote the location of maximum extratropical  $P - E$  in the climatology, and a similar comparison with  $P' - E'$  shows that there is a poleward shift in the extratropical  $P - E$  maximum. Siler et al. (2018) argued that polar amplification—which is a robust feature of global

warming—affects  $P' - E'$  by weakening the meridional temperature gradient and reducing poleward moisture transport. This helps to explain why there is reduced high-latitude  $P - E$  change and why the subtropical regions expand under warming in the MEBM and GCMs, when compared to the HS06 approximation. However, it is still unclear why the pattern of  $P' - E'$  from the MEBM is in better agreement with GCMs than Eq. (4) in the deep tropics, capturing increasing  $P - E$  in the deep tropics and a narrowing of the ITCZ region (Fig. 1a). Indeed, large-scale circulation features like the Hadley cells dominate latent energy transport in the deep tropics. This leads to a key question: How important are changes to the strength of the Hadley cells for  $P - E$  change in the tropics? Previous work (e.g., Byrne and Schneider 2016a,b) has shown that energetic arguments can be invoked to understand processes contributing to a narrowing of the ITCZ, but it remains unclear what energetic processes are driving these circulation changes and how these circulation changes relate to  $P - E$  changes (e.g., Chou et al. 2009; Chadwick et al. 2013). Other studies have also demonstrated that Hadley cell changes and ITCZ narrowing are likely related to radiative changes (Lau and Kim 2015; Su et al. 2014, 2019), but there remains a gap in our understanding of how these energetic constraints impact  $P - E$  changes.

Better understanding processes that set the pattern of  $P - E$  change may also help reduce uncertainty in future precipitation projections as sources of intermodel spread can be identified. Current GCMs exhibit a large intermodel spread in the pattern of  $P - E$  change under global warming, and the exact reasons for this spread remains unknown (Prein and Pendergrass 2019). Previous studies have shown that tropical radiative feedbacks contribute to uncertainty in the amount of warming that is nearly spatially uniform, while polar radiative feedbacks contribute to uncertainty in the amount of warming that is confined to the poles (Roe et al. 2015; Bonan et al. 2018). Yet, an important question remains unanswered: What processes constitute the greatest sources of uncertainty in the pattern of  $P - E$  change under climate change? The ability of the MEBM to emulate zonal-mean  $P - E$  change simulated by GCMs under greenhouse gas forcing (see Fig. 1a) suggests the MEBM can also be used to examine sources of uncertainty in  $P - E$  change.

In this paper, we have two specific aims:

- 1) We identify sources of intermodel spread in the pattern of  $P - E$  change under global warming. To do this, we first show that the MEBM is able to account for a majority of the intermodel variance in  $P - E$  change across a range of latitudes for GCMs under  $4 \times \text{CO}_2$ . We then link the intermodel spread in  $P - E$  change to radiative feedbacks, radiative forcing, and ocean heat uptake.
- 2) We further investigate differences between the simple thermodynamic perspective introduced by HS06 and the downgradient energy transport perspective introduced by Siler et al. (2018). Specifically, we use the MEBM to consider how the pattern of radiative feedbacks impacts the pattern of  $P - E$  change in the tropics and extratropics. We show that changes to the net heating of the atmosphere and gross moist stability act to strengthen and

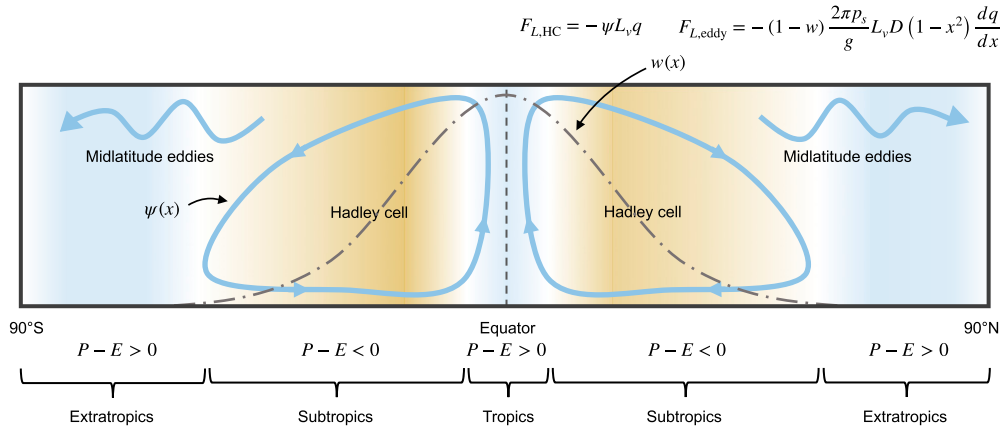


FIG. 2. Schematic depicting the moist energy balance model Hadley cell parameterization. A Gaussian weighting function  $w(x)$ , shown in the gray dash-dot line is used to partition atmospheric heat transport  $F(x)$  into a component due to the Hadley cell  $F_{\text{HC}}(x)$  and a component due to eddies  $F_{\text{eddy}}(x)$ . A streamfunction  $\psi$  is then approximated using assumptions about gross moist stability (see section 2 and appendix B);  $\psi$  is then used to flux moisture upgradient while the rest is diffused downgradient and modulated by the weighting function. By summing the two terms and taking the divergence, a pattern of  $P - E$  is obtained.

weaken the Hadley cell in different regions, which alters moisture transport to the tropics, narrows the ITCZ and increases  $P - E$  in the deep tropics. We also show how changes to the meridional temperature gradient alters poleward moisture transport.

The paper is structured as follows. In section 2, we describe the MEBM and Hadley cell parameterization. In section 3, we assess the skill of the MEBM in emulating GCMs under greenhouse gas forcing and use the MEBM to identify sources of uncertainty in the pattern of  $P - E$  change. In section 4, we examine how the pattern of radiative feedbacks impacts  $P - E$  changes in the deep tropics and extratropics using a set of simple scalings and compare these results to output from GCMs. Finally, in section 5, we discuss key results and implications of this work.

## 2. A modified moist energy balance model

A series of studies have shown that downgradient energy transport by the atmosphere is remarkably successful at emulating the zonal-mean climate, and its response to greenhouse gas forcing (Flannery 1984; Hwang and Frierson 2010; Roe et al. 2015; Siler et al. 2018; Bonan et al. 2018; Merlis and Henry 2018; Armour et al. 2019; Russotto and Biasutti 2020; Lutsko et al. 2020; Hill et al. 2022; Beer and Eisenman 2022). When applied to climate change, the MEBM assumes that the anomalous northward column-integrated atmospheric energy transport  $F'(x)$  is proportional to the meridional gradient of anomalous near-surface moist static energy  $h' = c_p T' + L_v q'$ , which gives

$$F'(x) = -\frac{2\pi p_s}{g} D(1-x^2) \frac{dh'}{dx}, \quad (5)$$

where  $c_p$  is the specific heat of air ( $1005 \text{ J kg}^{-1} \text{ K}^{-1}$ ),  $q'$  is the anomalous near-surface specific humidity (assuming fixed relative humidity of 80%),  $p_s$  is surface air pressure (1000 hPa),

$$F_{L,\text{HC}} = -\psi L_v q \quad F_{L,\text{eddy}} = -(1-w) \frac{2\pi p_s}{g} L_v D (1-x^2) \frac{dq}{dx}$$

$g$  is the acceleration due to gravity ( $9.81 \text{ m s}^{-2}$ ),  $D$  is a constant diffusion coefficient (with units of  $\text{m}^2 \text{ s}^{-1}$ ),  $x$  is sine latitude, and  $1 - x^2$  accounts for the spherical geometry.

Under warming, the anomalous heating of the atmosphere must be balanced by the divergence of  $F'(x)$ . We define  $R_f(x)$  as the local top-of-the-atmosphere (TOA) radiative forcing;  $\lambda(x)$  as the local radiative feedback, defined as the change in net upward TOA radiative flux per degree of local surface warming ( $\text{W m}^{-2} \text{ K}^{-1}$ ); and  $G'(x)$  as the change in net surface heat flux, which is equivalent to the divergence of ocean heat transport and ocean heat storage. Combining these three terms (i.e., the anomalous heating of the atmosphere) with the divergence of Eq. (5) gives

$$R_f(x) - G'(x) + \lambda(x)T'(x) = \nabla \cdot F'(x), \quad (6)$$

which is a single differential equation that can be solved numerically for  $T'(x)$  and  $F'(x)$  given patterns of  $R_f(x)$ ,  $G'(x)$ , and  $\lambda(x)$  and a value of  $D$ .

To simulate a realistic hydrological cycle, we follow Siler et al. (2018) and Armour et al. (2019) and define a Gaussian weighting function  $w(x)$  that partitions the transport of anomalous latent and dry static energy within the tropics. A schematic depicting the mean-state Hadley cell parameterization is shown in Fig. 2. We divide  $F'(x)$  into a component due to the Hadley cells  $F'_{\text{HC}}(x)$  and a component due to the eddies  $F'_{\text{eddy}}(x)$ , and define  $w(x)$  as the fraction of total energy transport that is accomplished by the Hadley cells at a given latitude:

$$F'_{\text{HC}}(x) = w(x)F'(x) \quad \text{and} \quad F'_{\text{eddy}}(x) = [1 - w(x)]F'(x), \quad \text{and} \quad (7)$$

$$w(x) = \exp\left(\frac{-x^2}{\sigma_x^2}\right), \quad (8)$$

where  $\sigma_x$  is a width parameter, which we set to 0.3 following Siler et al. (2018). In this formulation, eddies account for essentially all anomalous energy transport poleward of 45°S and 45°N, while the Hadley cell accounts for most anomalous energy transport between 10°S and 10°N. Note that this formulation explicitly leaves out representation of the extratropical components of the mean meridional circulation (i.e., Ferrel and polar cells) and does not allow for the extent of the Hadley cell to change under warming.

In the mean-state climate, poleward atmospheric heat transport by the Hadley cell  $F_{\text{HC}}(x)$  is equal to

$$F_{\text{HC}}(x) = \psi(x)H(x), \quad (9)$$

where  $\psi(x)$  is the mass transport ( $\text{kg s}^{-1}$ ) in each branch of the Hadley cell and  $H(x)$  is the gross moist stability, defined as the difference between  $h$  in the upper and lower branches at each latitude (see details below). However, because we are considering  $P - E$  change under warming, the anomalous poleward atmospheric heat transport by the Hadley cell is represented as

$$F'_{\text{HC}}(x) = \psi'(x)\bar{H}(x) + \bar{\psi}(x)H'(x) + \psi'(x)H'(x), \quad (10)$$

where  $\psi'(x)$  is the anomalous mass transport ( $\text{kg s}^{-1}$ ) in each branch of the Hadley cell and  $H'(x)$  is the anomalous gross moist stability (i.e., the difference between  $h'$  in the upper and lower branches at each latitude). Note that we have written Eq. (10) in terms of a perturbation around the climatological mean-state. Appendix B details how the climatological state is approximated using the MEBM. In sections 3 and 4, we use the climatological state of each GCM when doing CMIP5 comparisons. For the idealized analyses of section 4, the climatological state is equivalent to the multimodel mean climatological state of the 20 CMIP5 GCMs under preindustrial conditions, but symmetric about the equator so as not to introduce hemispheric asymmetries. Note, for the idealized analysis, we make the control fields symmetric about the equator to isolate the impact of the radiative feedback pattern only.

Following Held (2001) and Merlis et al. (2013), we assume that anomalous upper tropospheric moist static energy is uniform in the tropics (e.g., Raymond et al. 2009) with a constant value of  $h'_0$ . Thus, variations in  $H'(x)$  are due entirely to meridional variations in  $h'$  giving  $H'(x) \approx h'_0 - h'(x)$ , where  $h'_0 = 1.08 \times h'(0)$ , or 8% above  $h'$  at the equator ( $x = 0$ ). Note that this value is slightly higher than the value used by Siler et al. (2018), which is 6% above  $h'$  at the equator, but was found to better emulate  $P - E$  change in GCMs. Each GCM uses the same scaling factor. Higher scaling factors result in weaker Hadley cell mass fluxes and less tropical  $P - E$ . The anomalous latent energy transport by the Hadley cell  $F'_{L,\text{HC}}(x)$  is thus

$$F'_{L,\text{HC}}(x) = -[\psi'(x)L_v\bar{q}(x) + \bar{\psi}(x)L_vq'(x) + \psi'(x)L_vq'(x)]. \quad (11)$$

The assumption about moisture transport holds because the upper branch of the Hadley cell is essentially dry, meaning

anomalous latent energy transport is confined to the lower branch. With this simple Hadley cell parameterization, the anomalous latent energy transport can be obtained by summing the terms due to the Hadley cells and eddies:

$$F'_L(x) = F'_{L,\text{HC}}(x) + F'_{L,\text{eddy}}(x), \quad (12)$$

where

$$F'_{L,\text{eddy}}(x) = -(1-w)\frac{2\pi p_s}{g}L_vD(1-x^2)\frac{dq'}{dx}. \quad (13)$$

The divergence of  $F'_L(x)$  [Eq. (12)] then yields the change in  $P - E$ :

$$P' - E' = -\nabla \cdot F'_L(x) = -\frac{1}{2\pi a^2} \frac{dF'_L}{dx}. \quad (14)$$

The essential feature of the MEBM framework is that it allows for a self-consistent representation of atmospheric heat transport, while allowing us to examine how different factors, such as the patterns of  $\lambda$ ,  $G'$ ,  $R_f$ , and  $T'$  impact that pattern of  $P' - E'$ . It also important to note this framework ensures that  $P' = E'$  globally. In the next section, we compare the HS06 approximation and the MEBM solution. The HS06 approximation and the MEBM both contain three inputs. The HS06 approximation uses the pattern of temperature change, the pattern (or value) of the Clausius–Clapeyron scaling factor, and the climatological pattern of  $P - E$ ; while the MEBM uses the pattern of radiative feedbacks, the pattern of radiative forcing, and the pattern of ocean heat uptake and assumes that downgradient energy transport can be used to predict  $P - E$  change.

### 3. Changes to the hydrological cycle in a moist energy balance model

We first assess the ability of the MEBM to emulate a suite of comprehensive GCMs under greenhouse gas forcing largely following Siler et al. (2018). To do this, we compute the model-specific patterns of  $R_f$ ,  $G'$ , and  $\lambda$  from 20 different CMIP5 GCMs (see appendix A) and calculate the  $P' - E'$  pattern from the MEBM defined in section 2. Note, for this section we use model-specific values of  $D$  and model-specific climatological states from a climatological version of the MEBM (see appendix B).

Figure 3 shows the pattern of  $P - E$  change from each GCM, the MEBM solution, and the HS06 approximation. While the overall pattern of “wet-gets-wetter, dry-gets-drier” is similar across both the HS06 approximation and MEBM, there is much better agreement between GCMs and the MEBM than between GCMs and the HS06 approximation. For example, in GCMs with large values of  $P' - E'$  in the deep tropics (e.g., ACCESS-1.0, CanESM2, CSIRO-Mk3.6.0, and MIROC-ESM) there is a good agreement between the MEBM and GCMs that is not captured by the HS06 approximation, suggesting that the MEBM is capturing changes in latent energy transport that the HS06 approximation leaves out. The MEBM also captures a narrowing of the ITCZ

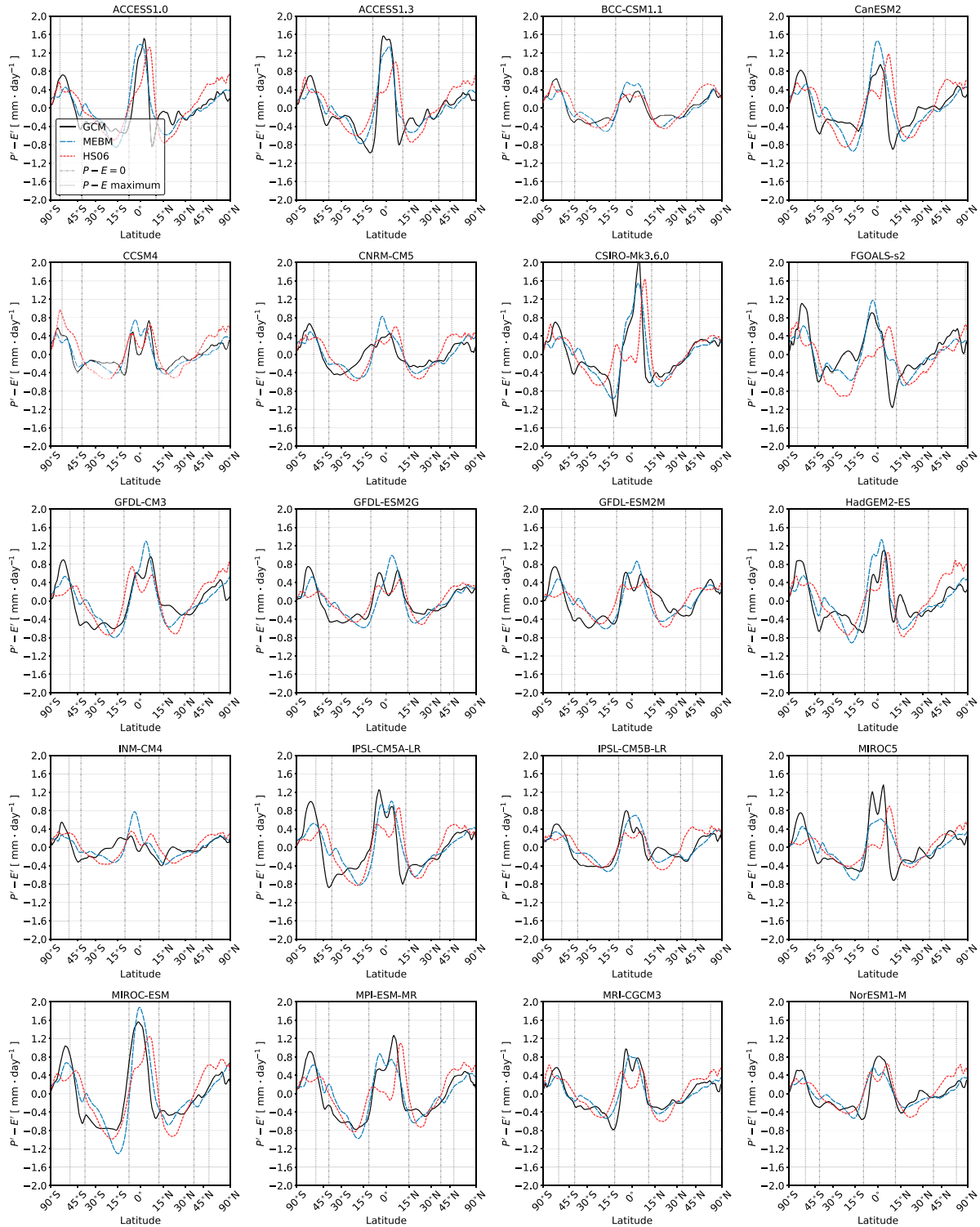


FIG. 3. Response of the hydrological cycle to global warming in a moist energy balance model. The pattern of  $P' - E'$  in 20 CIP5 simulations 126–150 years after an abrupt quadrupling of  $\text{CO}_2$ . The black line denotes the GCM, the blue line denotes the MEBM solution, and the red line denotes the HS06 approximation. The gray dashed vertical lines represent the  $P - E = 0$  boundary in the climatology, which corresponds to the subtropical regions; and the gray dotted vertical lines represent the extratropical  $P - E$  maximum, which is a measure of the latitude of the storm tracks. Changes in subtropical boundaries and storm-track latitude can be inferred by comparing the  $P' - E'$  changes with these vertical lines.

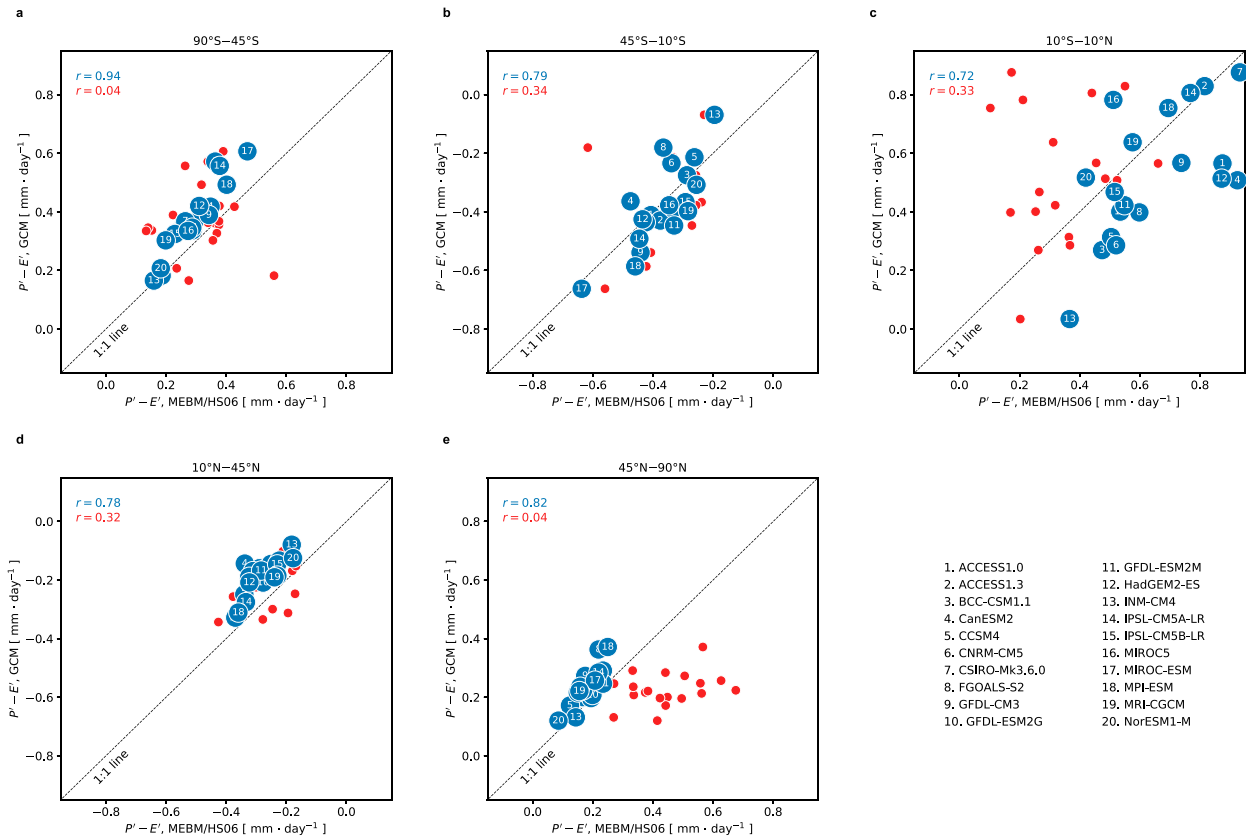


FIG. 4. Skill of the moist energy balance model. Scatterplots of the area-averaged  $P - E$  in the GCM, HS06 approximation (red), and MEBM (blue) for (a) 90°–5°S, (b) 45°–10°S, (c) 10°S–10°N, (d) 10°–45°N, and (e) 45°–90°N. The top-left corner of each plot shows the Pearson correlation coefficient between the  $P - E$  responses from the MEBM and GCM (blue) and HS06 and GCM (red).

region, which occurs in every GCM analyzed here, and can be inferred from Fig. 3 because  $P - E$  is negative at the equatorward climatological  $P - E = 0$  line (dash-dot line in each panel). In the extratropical regions, the MEBM captures, better than the HS06 approximation, the more muted  $P - E$  change also shown by GCMs (e.g., ACCESS-1.3, CCSM4, HadGEM2-ES). The MEBM also broadly captures the expansion of the subtropical regions in each GCM.

To quantitatively compare the  $P - E$  change from each individual GCM, the MEBM solution, and the HS06 approximation, we take area-weighted averages of  $P - E$  change in five distinct regions that represent the extratropics (90°–45°S and 45°–90°N), the subtropics (45°–10°S and 10°–45°N) and the deep tropics (10°S–10°N). In the extratropics, the MEBM accounts for approximately 70% of the intermodel variance while the HS06 approximation accounts for effectively none (Figs. 4a,e). In the subtropics, the MEBM accounts for less intermodel variance ( $r^2 \approx 0.60$ ; Figs. 4b,d), but still far more than the HS06 approximation ( $r^2 \approx 0.10$ ). In the deep tropics, where the MEBM solution predicts larger increases in  $P - E$  when compared to the HS06 approximation, the MEBM accounts for approximately 50% of the intermodel variance,

compared with about 10% for the HS06 approximation (Fig. 4c).

#### a. Sources of uncertainty

Having demonstrated that the MEBM emulates the zonal-mean  $P - E$  change for each individual GCM, we next investigate the reason for the good agreement between the MEBM and GCMs, and the intermodel spread in the zonal-mean  $P - E$  change. Uncertainty in the MEBM mainly arises from three sources: radiative forcing  $R_f$ , ocean heat uptake  $G'$ , and radiative feedbacks  $\lambda$ . Following Bonan et al. (2018), we disaggregate the  $P - E$  change into separate contributions from  $R_f$ ,  $G'$ , and  $\lambda$  by creating a baseline pattern of  $P - E$  for the MEBM using the multimodel mean patterns of  $R_f$ ,  $G'$ , and  $\lambda$ . We then run the MEBM using the GCM-specific patterns of either  $R_f$ ,  $G'$ , and  $\lambda$  (Fig. A1) while holding the other two variables fixed at their multimodel mean patterns. This generates a spread of MEBM  $P - E$  patterns due to intermodel differences in either  $R_f$ ,  $G'$ , and  $\lambda$ . To understand the relative importance of each contributing factor, we calculate the variance of  $P - E$  as a function of latitude from each individual factor. We then compute the fractional contribution of each factor to the total variance by assuming

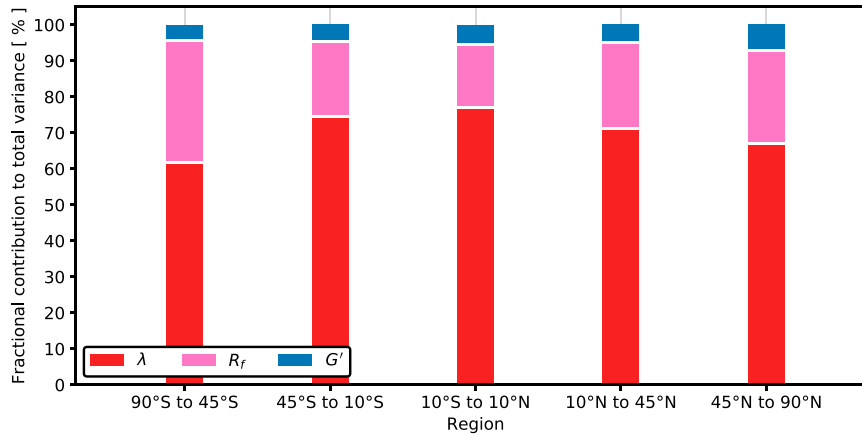


FIG. 5. Sources of uncertainty in the response of the hydrological cycle to global warming in different regions. Fractional contribution of  $\lambda$ ,  $R_f$ , and  $G'$  to the total variance in  $P' - E'$  for averages over 90°–45°S, 45°–10°S, 10°S–10°N, 10°–45°N, and 45°–90°N.

that the variance associated with each factor can be added linearly.

Figure 5 shows the fractional contribution of  $R_f$ ,  $G'$ , and  $\lambda$  to the total variance in  $P' - E'$  for the same regions described above. Across all regions intermodel variations in  $\lambda$  are the leading cause of intermodel variations in  $P' - E'$ , accounting for 60%–75% of the intermodel variance. In the extratropical regions, the contribution of  $\lambda$  to the intermodel spread in  $P' - E'$  is smaller than in the tropics (Fig. 5). The  $R_f$  accounts for 15%–30% of the intermodel variance in  $P' - E'$  patterns, and accounts for more intermodel variance in the extratropical regions when compared to the tropics. Intermodel variations in  $G'$  account for 5%–8% of the intermodel variance across all regions. Note that these averages represent broad swaths of  $P' - E'$ , which exhibits large spatial variations as a function of latitude. The same analysis as a continuous function of latitude yields a greater influence of  $G'$  at some latitudes, accounting for approximately 30%–40% of the intermodel variance in  $P' - E'$  in regions of large ocean heat uptake, such as the North Atlantic and Southern Ocean (Marshall et al. 2015).

#### b. Local and remote impacts of climate feedbacks

Given that the intermodel spread of  $\lambda$  is the main source of uncertainty in the pattern of  $P' - E'$ , we next consider the relative importance of  $\lambda$  in different regions. The remote-versus-local influence of  $\lambda$  has been shown to be an important factor when considering uncertainty in the pattern of temperature change (Roe et al. 2015; Bonan et al. 2018), but its influence on  $P - E$  change is less understood. To examine this, we run the MEBM with the multimodel mean patterns of  $R_f$  and  $G'$ , and confine the intermodel spread of  $\lambda$  to the tropics (30°S–30°N) and extratropics (90°–30°S and 30°–90°N) while the other region is set to the multimodel mean of  $\lambda$ . This isolates the impact of  $\lambda$  uncertainty in one region on  $P' - E'$  uncertainty in other regions, but does not isolate interhemispheric changes. Note that these regions span equal areas of the globe.

Figure 6 shows the fractional contribution of intermodel variations of  $\lambda$  in the tropical and extratropical regions to the

total variance in  $P' - E'$  for the same regions examined above. In the deep tropics and subtropics, intermodel differences in tropical  $\lambda$  account for 85%–92% of intermodel variance in  $P' - E'$ . In the extratropical regions, intermodel differences in tropical  $\lambda$  contribute to approximately 60% of the intermodel variance in  $P' - E'$ . Notably, intermodel variations in  $\lambda$  in the extratropical regions contribute little to intermodel variations in  $P' - E'$  in the deep tropics and subtropics, but contribute approximately 40% of the intermodel variations of  $P - E$  in the extratropical regions. This is similar to the results of Bonan et al. (2018), where tropical-feedback uncertainty was found to contribute to warming uncertainty that was nearly uniform with latitude.

#### 4. Impact of radiative feedback patterns on hydrological changes

Having shown that the MEBM emulates zonal-mean  $P - E$  change simulated by GCMs under greenhouse gas forcing with high skill, and this change is largely determined by radiative feedbacks, we now use the MEBM with idealized radiative-feedback patterns and a set of simple scalings to investigate the specific mechanisms responsible for the zonal-mean  $P - E$  change. The radiative-feedback patterns are constructed to illustrate key differences between the MEBM and HS06 approximation. Note that the pattern of  $P' - E'$  from the HS06 approximation is purely thermodynamic, arising from the climatological pattern of  $P - E$  and the spatial pattern of warming, whereas the pattern of  $P' - E'$  from the MEBM is both thermodynamic and dynamic, arising from changes in latent energy transport from eddies and the Hadley cells, both of which are constrained by the overall energetic demand in the atmosphere.

##### a. Experiments and overview

We first set  $G'(x) = 1.54 \text{ W m}^{-2}$  and  $R_f(x) = 6.35 \text{ W m}^{-2}$ , which are the multimodel and global-mean values of the CMIP5 GCMs. The  $D$  term is set to  $1.05 \times 10^6 \text{ m}^2 \text{ s}^{-1}$ , which is the multimodel mean value of the CMIP5 GCMs. We also



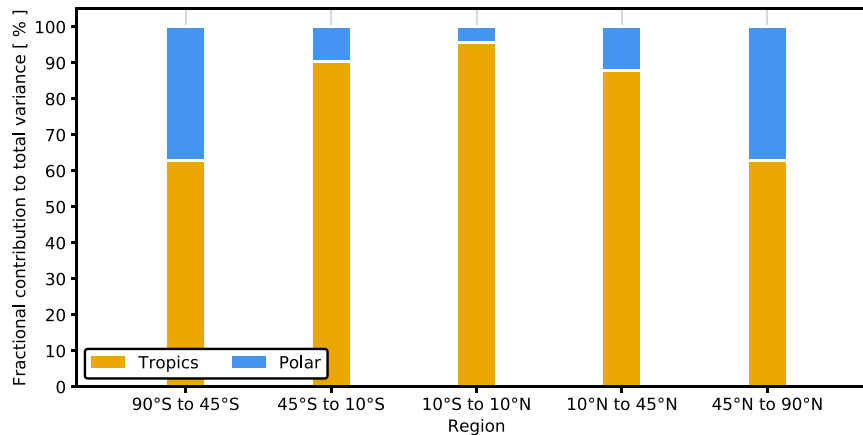


FIG. 6. Local and remote influence of regional climate feedbacks on the response of the hydrological cycle to global warming. Fractional contribution of intermodel variations of  $\lambda$  in the tropical (30°S–30°N) and extratropical regions (90°–30°S and 30°–90°N) to the total variance in  $P' - E'$  for averages over 90°–45°S, 45°–10°S, 10°S–10°N, 10°–45°N, and 45°–90°N.

take the multimodel mean climatological MEBM variables ( $\psi$ ,  $H$ ,  $T$ ) and make them symmetric about the equator. Thus, any asymmetries in the idealized analyses of section 4 result from asymmetries in the pattern of radiative feedbacks only. Next, we create four  $\lambda$  patterns that broadly represent the intermodel spread of CMIP5 GCMs (see Fig. A1) and produce four distinct patterns of warming (Fig. 7). These patterns are as follows:

- 1) The first  $\lambda$  pattern is weakly negative in the deep tropics, positive in the subtropics, and negative in the extratropics (Fig. 7a). This  $\lambda$  pattern produces a pattern of warming that is uniform with latitude and equivalent to the multimodel and global-mean value of warming from the CMIP5 GCMs. This pattern was calculated by prescribing a uniform  $T'$  in Eq. (6) and solving for  $\lambda$ .
- 2) The second  $\lambda$  pattern is uniform with latitude and equivalent to the multimodel and global-mean value of  $\lambda$  from the CMIP5 GCMs (Fig. 7b). This  $\lambda$  pattern produces a pattern of warming that is polar amplified in both hemispheres and contains little-to-no structure in the deep tropics.
- 3) The third  $\lambda$  pattern is symmetric across both hemispheres but contains a narrowly positive peak value of  $\lambda$  in the deep tropics and negative values elsewhere (Fig. 7c). This pattern was calculated by taking the pattern of  $\lambda$  from CSIRO-Mk3.6.0, which exhibits the largest increases in  $P - E$  in the deep tropics, and making it symmetric across the equator. This  $\lambda$  pattern produces a pattern of warming that is also polar amplified in both hemispheres, but contains a slight amplification of warming near the equator.
- 4) The fourth  $\lambda$  pattern is antisymmetric across both hemispheres but still contains a narrowly positive peak value of  $\lambda$  in the deep tropics and negative values elsewhere (Fig. 7d). This  $\lambda$  pattern is from CSIRO-Mk3.6.0 and produces a pattern of warming that is more polar-amplified in the Arctic and less polar amplified in the Antarctic, but

also contains a slight amplification of warming near the equator.

The resulting patterns of  $P' - E'$  are shown in the right columns of Fig. 7, along with a comparison to the HS06 approximation. We briefly describe the patterns, before analyzing the causes in the next two subsections, focusing separately on the tropics and extratropics. For pattern 1, when  $\lambda$  is mostly positive in the subtropics and negative in the extratropics (Fig. 7a), the pattern of warming is uniform. This results in a  $P' - E'$  pattern that is nearly identical to the HS06 approximation [i.e., Eq. (4)], with increasing  $P - E$  in the tropics and high latitudes and decreasing  $P - E$  in the subtropics. Note that this  $P - E$  pattern contains no change in the subtropical boundaries or narrowing of the ITCZ. However, for pattern 2, when  $\lambda$  is uniform with latitude, there is a polar-amplified pattern of warming, which results in a pattern of  $P' - E'$  that is different between the MEBM and HS06. For polar-amplified warming, while the pattern of  $P' - E'$  for the MEBM and HS06 approximation is similar in the tropics,  $P' - E'$  in the extratropics and subtropics is much muted in the MEBM. Finally, for pattern 3 and pattern 4, when  $\lambda$  is narrowly positive in the deep tropics and negative across most other latitudes, there is a similar difference between the MEBM and HS06  $P' - E'$  in the high latitudes, but the MEBM  $P' - E'$  is larger in the deep tropics. This increase in the deep tropics far exceeds the HS06 approximation [Eq. (4)], and coincides with a narrowing of the ITCZ where  $P - E > 0$ .

To provide a more mechanistic interpretation of how the pattern of  $\lambda$  impacts the pattern of  $P' - E'$ , in the next two subsections we compare the MEBM and HS06 approximation using a set of simple scalings.

#### b. Tropics

In Figs. 1 and 3 we saw that, in the tropics,  $P - E$  change in the MEBM is much larger than  $P - E$  change in the HS06

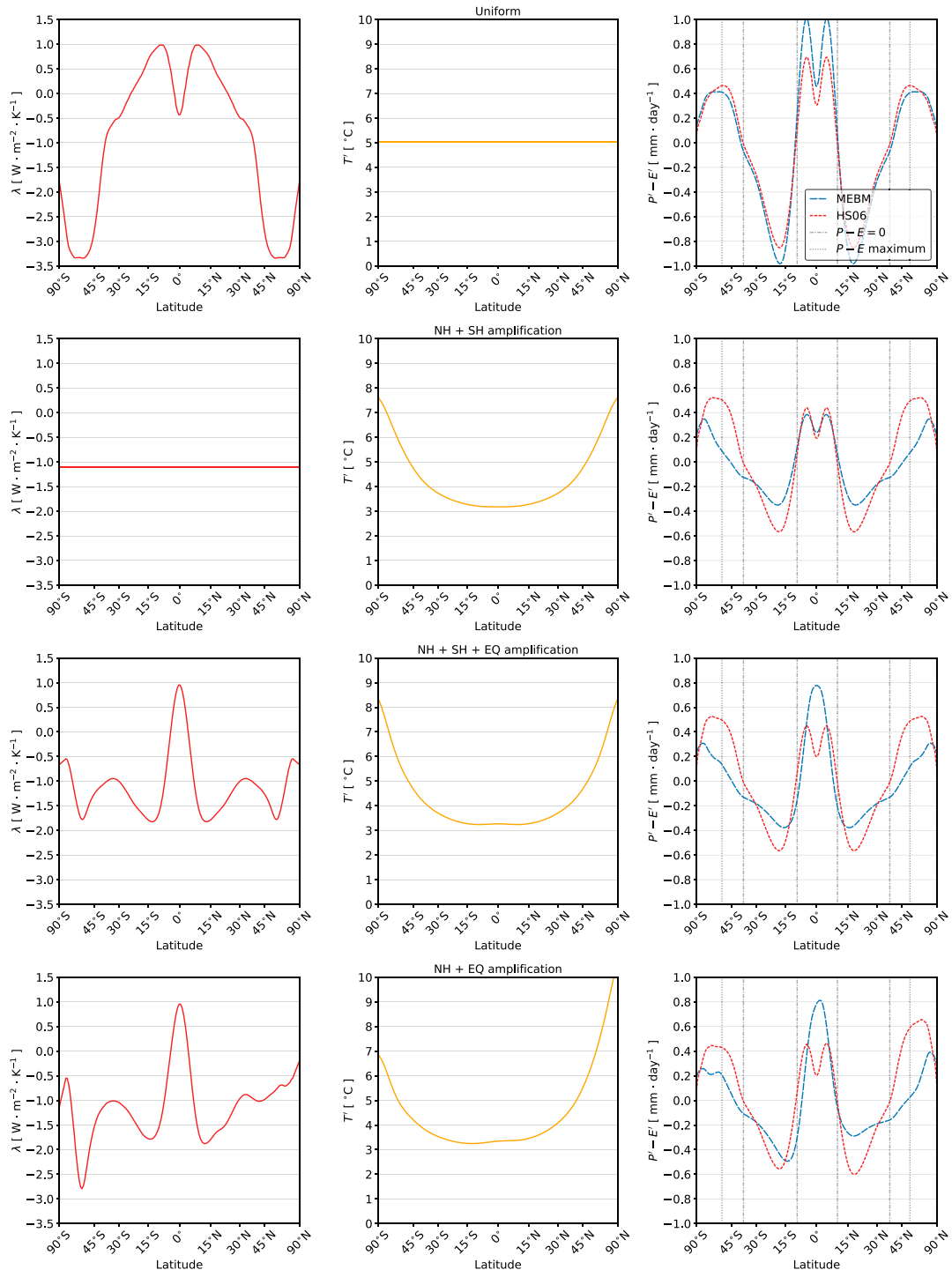


FIG. 7. Impact of radiative feedback patterns on the response of the hydrological cycle to global warming. (left) A pattern of the net radiative feedback that induces (center) a pattern of warming: 1) that is uniform, 2) with equal degrees of polar amplification in the Northern Hemisphere and Southern Hemisphere, 3) with equal degrees of polar amplification in the Northern Hemisphere and Southern Hemisphere and amplified warming on the equator, and 4) with more polar amplification in the Northern Hemisphere than Southern Hemisphere and amplified warming on the equator. (right) The pattern of  $P - E$  for each pattern of the net radiative feedback. The blue dashed line denotes the MEBM solution, and the red dashed line is the HS06 approximation assuming  $\alpha = 7\% \text{ K}^{-1}$  globally and using the multimodel mean climatological pattern of  $P - E$  from 20 preindustrial control simulations, which is shown in Fig. 1c. Note that the climatological patterns have been symmetrized about the equator.

approximation, and is in much better agreement with GCMs. This is also evident in Fig. 7 with the idealized radiative feedback patterns. These differences are likely related to the fact that the MEBM contains a Hadley cell parameterization which simulates changes to the Hadley cell circulation strength under warming. Thus, differences between the MEBM and HS06 approximation in the deep tropics can be understood through the conservation statement for the atmospheric-moisture budget for  $P - E$  under warming:

$$(P' - E')_{\text{HC}} = -\nabla \cdot (\bar{\psi} L_v q' + \psi' L_v \bar{q} + \psi' L_v q'), \quad (15)$$

where  $(\bar{\cdot})$  represents the climatological state. Here,  $\bar{\psi}$  and  $\bar{q}$  are derived by applying the MEBM to each preindustrial control simulation from 20 GCMs (see appendix B for details). This enables us to decompose  $P' - E'$  in the MEBM—for regions where the Hadley cell accomplishes most of the latent-energy transport—into thermodynamic and dynamic contributions to  $P' - E'$ . Broadly, the first term represents no changes to the strength of the Hadley cell and changes to the moisture content of the atmosphere [which is nearly equivalent to Eq. (4)]; the second term represents changes to the strength of the Hadley cell and no changes to the moisture content of the atmosphere; and the third term is second order and combines changes to the strength of the Hadley cell and moisture changes.

Figure 8 shows  $P' - E'$  for each pattern of  $\lambda$  into contributions from the three terms in Eq. (15), in the region influenced by the Hadley cells (45°S–45°N). Under a uniform pattern of warming (Fig. 8a) the thermodynamic term (red dotted line) dominates  $P' - E'$  while the two dynamical terms (purple line) simply amplify the existing pattern of  $P - E$ , with no change in the spatial structure of  $P - E$ . Note that the thermodynamic term, which does not represent changes to the strength of the Hadley cell, is nearly equivalent to the HS06 approximation in the deep tropics. Similarly, under a pattern of warming with equal degrees of polar amplification in each hemisphere and uniform warming throughout the tropics (Fig. 8b), the thermodynamic term (red dotted line) again dominates  $P' - E'$  and there is little-to-no change in the spatial pattern of  $P - E$  in the deep tropics from the dynamical terms (purple line). However, under a pattern of warming with equal degrees of polar amplification in each hemisphere (Fig. 8c), but more warming near the equator, the dynamical terms dominate  $P - E$  changes in the deep tropics. Here,  $\psi'$  causes an enhancement of  $P - E$  in the deep tropics. Between 5°S and 5°N, changes to  $\psi$  contribute to an enhancement of approximately 0.5 mm day<sup>-1</sup> in  $P - E$ . Likewise, under amplified warming of the Arctic, more muted Southern Hemisphere warming, and amplified warming near the equator (Fig. 8d), there is larger  $P - E$  in the deep tropics, which also arises mainly from changes in  $\psi$ .

Because the Hadley cells greatly impact  $P - E$  change in the deep tropics, we now focus on the mechanisms responsible for the mass-flux changes in the MEBM. To do this, we turn to Eq. (10), which relates the strength of the Hadley cell to the poleward heat flux and gross moist stability. Rearranging for  $\psi'(x)$  gives

$$\psi'(x) = \frac{F'_{\text{HC}}}{\bar{H} + H'} - \frac{\bar{\psi} H'}{\bar{H} + H'}, \quad (16)$$

$\psi'_1$    $\psi'_2$

where  $\psi'_1$  represents changes to  $\psi$  that result from changes in the poleward heat transport by the Hadley cell and  $\psi'_2$  represents changes to  $\psi$  that result from changes in gross moist stability, or the stratification of the tropical atmosphere. Note that gross moist stability always scales at 8% above the equator value of  $h'_0$ , but can change due to changes in  $h'$ . These two terms can be combined with Eq. (15) to produce

$$(P' - E')_{\text{HC}} = -\nabla \cdot \left[ \bar{\psi} L_v q' + \underbrace{(\psi'_1 L_v \bar{q} + \psi'_1 L_v q')}_{\text{term 1}} + \underbrace{(\psi'_2 L_v \bar{q} + \psi'_2 L_v q')}_{\text{term 2}} \right], \quad (17)$$

where now  $P' - E'$  can be decomposed into three terms: a thermodynamic term with no circulation strength changes but changes to the moisture content of the atmosphere [i.e., Eq. (4)], and two dynamic terms that represent circulation strength changes from either the poleward heat transport by the Hadley cell (term 1) or changes in gross moist stability (term 2).

Figure 9 shows the divergence of anomalous atmospheric heat transport (Fig. 9a) and anomalous gross moist stability (Fig. 9b) for each of the four  $\lambda$  patterns. These two variables can be used to decompose changes to the Hadley cell circulation strength into the two terms from Eq. (16) (see Figs. 9c,d). The decomposition shows that changes to the poleward heat transport by the Hadley cell (i.e., term 1) largely act to strengthen  $\psi$ , and that changes to gross moist stability (i.e., term 2) largely act to weaken  $\psi$  (Fig. 9). With a pattern of  $\lambda$  that produces uniform warming there is excess energy in the tropics that must be exported poleward (see solid gold line in Fig. 9a), driving a stronger  $\psi$  (see solid gold line in Fig. 9c). Uniform warming also acts to produce the largest gross moist stability changes (see solid gold line in Fig. 9b), which weakens  $\psi$  (see solid gold line in Fig. 9d). The changes in gross moist stability are consistent with Chou et al. (2013), who found that increases in gross moist stability are related to a weakening of  $\psi$ . However, these changes are much smaller than the poleward heat changes and there is no change in the spatial structure of  $\psi'$  and therefore  $P' - E'$  increases largely following the climatological state (see solid gold line in Figs. 9e,f). This is also true for a uniform pattern of  $\lambda$ , where there are smaller changes to  $\psi$ , but again little-to-no change to the spatial structure of  $\psi$  (see dashed gold line in Figs. 9c,d).

With a pattern of  $\lambda$  that is less negative in the tropics and much more narrowly peaked—which is similar to the patterns of  $\lambda$  in GCMs—a different story emerges. Here, the small bump in warming in the deep tropics leads to an excess of energy in the deep tropics (see green lines in Fig. 9a). This drives a stronger Hadley cell in the deep tropics because of an increasing poleward heat flux (see green lines in Fig. 9c). The excess energy of the deep tropics cannot be radiated away

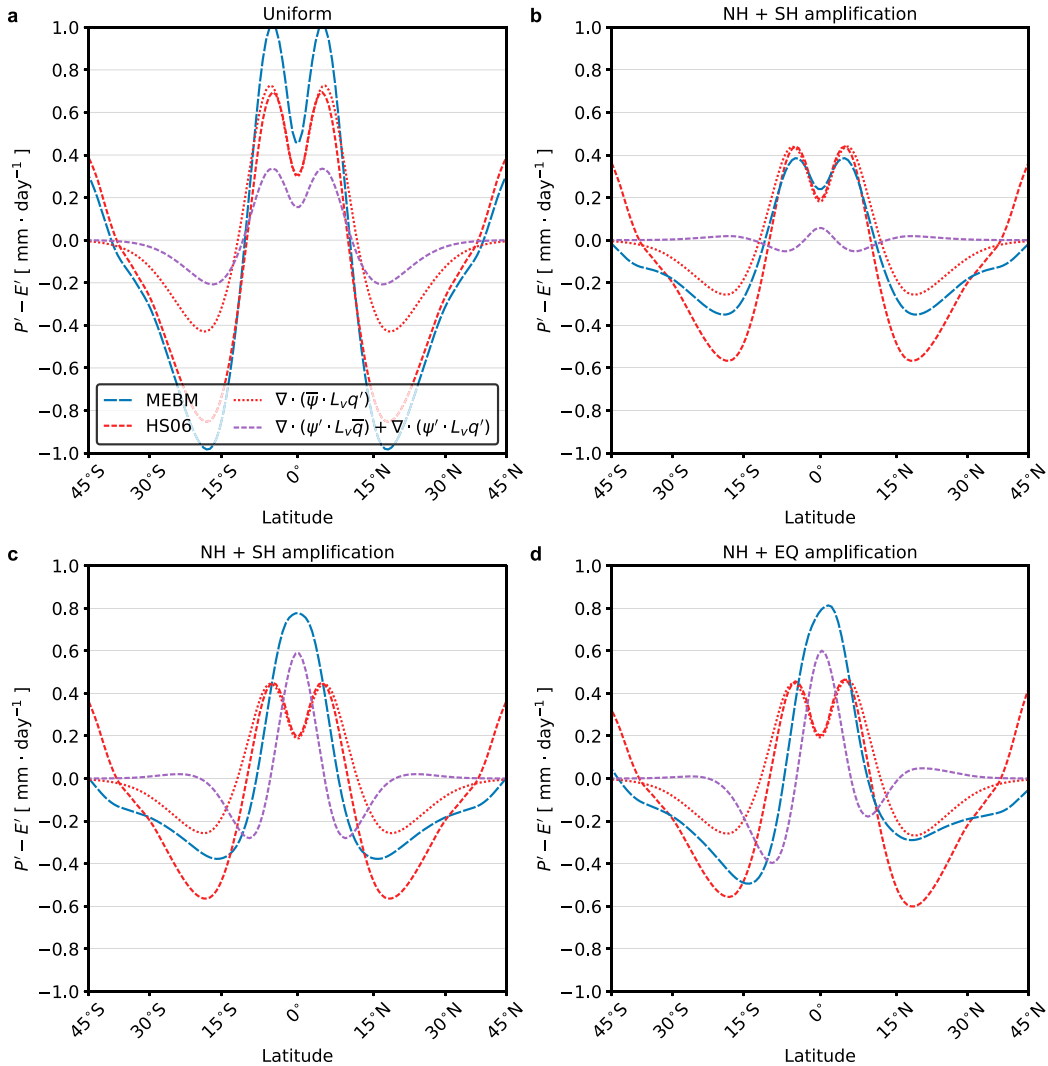


FIG. 8. Impact of radiative feedback patterns on the tropical hydrological cycle response. The pattern of  $P' - E'$  between  $45^{\circ}\text{S}$  and  $45^{\circ}\text{N}$  for a pattern of warming (a) that is uniform, (b) with equal degrees of polar amplification in the Northern Hemisphere and Southern Hemisphere, (c) with equal degrees of polar amplification in the Northern Hemisphere and Southern Hemisphere and amplified warming on the equator, and (d) with more polar amplification in the Northern Hemisphere than Southern Hemisphere and amplified warming on the equator. These are calculated following section 4a (see Fig. 7). The blue dashed line denotes the MEBM solution. The red dashed line denotes the HS06 approximation assuming  $\alpha = 7\% \text{ K}^{-1}$  globally. The red dotted line is the  $P' - E'$  pattern with no circulation strength changes and changes to the moisture content of the atmosphere,  $\nabla \cdot (\bar{\psi} \cdot L_v q')$ . The purple dashed line is the  $P' - E'$  pattern with circulation strength changes and changes to the moisture content of the atmosphere,  $\nabla \cdot (\psi' \cdot L_v \bar{q}) + \nabla \cdot (\bar{\psi} \cdot L_v q')$ . Note that the latitude range is confined to  $45^{\circ}$  as this is where the Hadley cell parameterization exhibits little-to-no influence on moisture transport.

locally and must be exported to higher latitudes, or regions of more efficient radiative loss. However, the structure of  $\lambda$  determines where this energy can go and hence the response of  $\psi$ : strengthening  $\psi$  in the deep tropics more than  $\psi$  in the subtropics (see green lines Fig. 9c). In other words, the fact that  $\lambda$  peaks near the equator and tapers off toward the subtropics means that  $\psi$  strengthens slightly more in the deep tropics relative to the subtropics, helping to change its spatial structure (Fig. 9c). Furthermore, because  $R_f$  and  $G'$  are spatially

uniform, any spatial structure in  $\lambda$  must be balanced by the spatial structure of  $\nabla \cdot F'_{\text{HC}}$  or  $T'$ . And because  $\nabla \cdot F'_{\text{HC}}$  contains more spatial structure than  $T'$ , the pattern of  $\lambda$  ultimately drives the  $P' - E'$  changes through the pattern of  $\nabla \cdot F'_{\text{HC}}$ . The change to the spatial structure of  $\psi$  patterns to increase  $P' - E'$  in the deep tropics and decrease  $P' - E'$  in the subtropics, which narrows the ITCZ region (Fig. 9e).

Term 2, which represents changes to  $\psi$  from gross moist stability changes, is small and cannot oppose the changes to  $\psi$  in

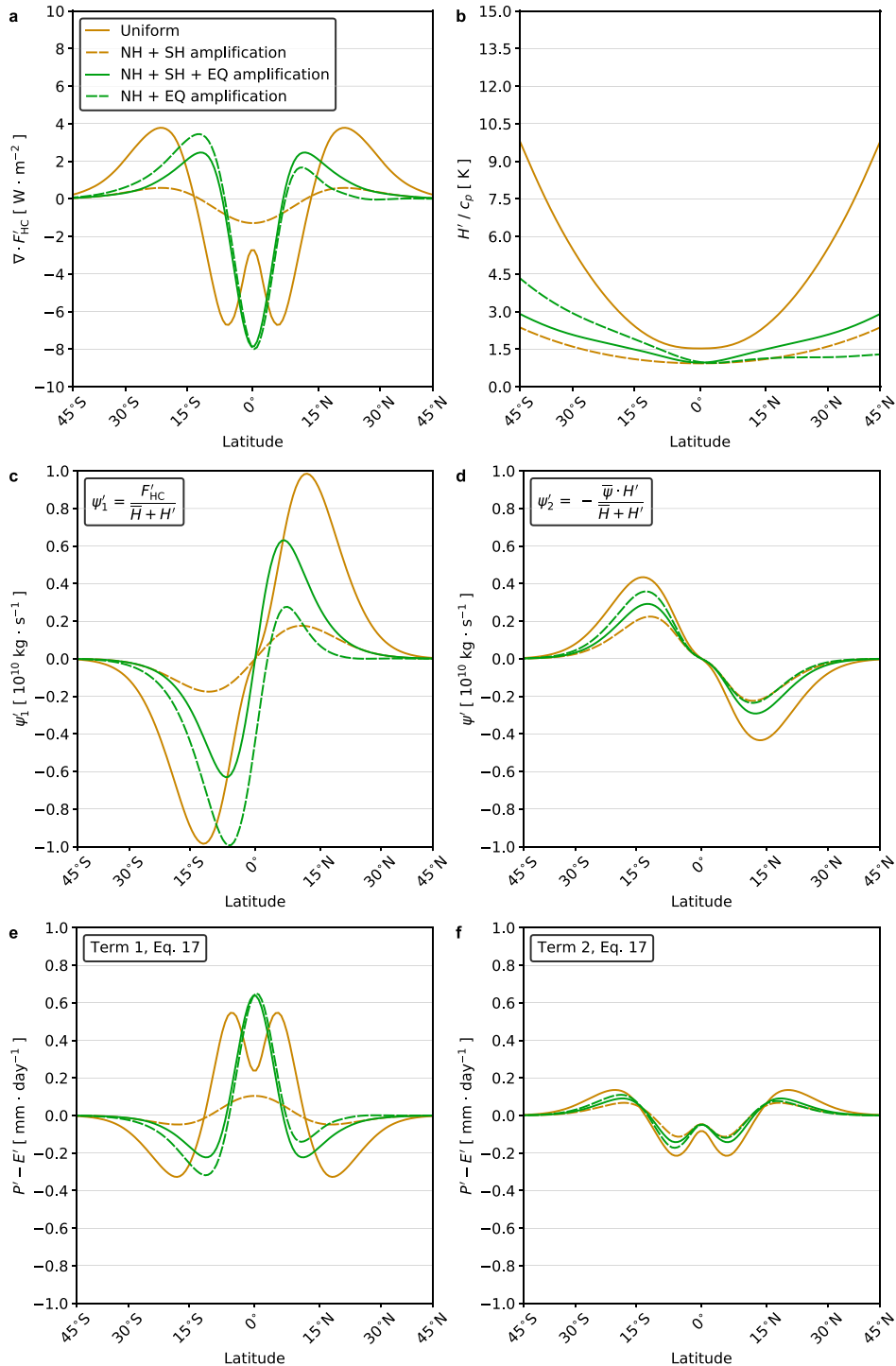


FIG. 9. Mechanisms for the influence of radiative feedbacks on the response of the tropical hydrological cycle. Changes to (a) the divergence of atmospheric energy transport by the Hadley cells ( $\nabla \cdot F'_{HC}$ ) and (b) gross moist stability ( $H'$ ). Changes to the northward mass transport by the parameterized Hadley cells, which is the sum of changes due (c) to the net atmospheric energy transport and (d) to gross moist stability changes.  $P - E$  changes (e) from term 1 and (f) term 2 from (c) and (d), respectively [see Eq. (17)]. The gold solid line denotes the uniform warming case. The gold dashed line denotes the polar-amplified warming case. The green solid line denotes the polar-amplified warming and equator warming case. The green dashed line denotes the Arctic-amplified warming and equator warming case.

the deep tropics that results from changes to the poleward heat transport by the Hadley cell (Fig. 9d). However, in the subtropics the weakening of  $\psi$  outcompetes the strengthening of  $\psi$  from an increase poleward heat flux (cf. Figs. 9c,d). The weakening of  $\psi$  from term 2 acts to decrease  $P - E$  at the edges of the ITCZ region (Fig. 9f). In other words, the pattern of radiative feedbacks causes anomalous energy to be exported from the tropics to the poles, strengthening  $\psi$ . At the same time, the increase in gross moist stability weakens  $\psi$ , but this weakening is confined mainly to the subtropics. This occurs because of larger increases to the moist static energy gradient in the subtropics when compared to the tropics. Together, in unison, these two processes determine the degree of ITCZ contraction. These circulation changes are similar to Feldl and Bordoni (2016), where the Hadley cell was found to strengthen in the deep tropics and weaken in the subtropics under warming. In section 4d we directly compare the mass-flux changes in the MEBM and GCMs.

### c. Extratropics

In the extratropics,  $P - E$  change from the MEBM and the HS06 approximation are approximately equal under uniform warming (Fig. 7a), but are different under polar-amplified warming (Figs. 7b–d). Under polar-amplified warming the MEBM predicts less enhancement of high-latitude  $P - E$  than HS06, and is in better agreement with the GCMs (see Figs. 1a and 3). The MEBM also predicts an expansion of the subtropical regions (see sections 1 and 3). To understand how these differences arise, we use an extended version of the simple scaling from HS06, which is detailed in Siler et al. (2018). Appendix C contains relevant details of the derivation, but this scaling decomposes  $P' - E'$  in the extratropics into two terms via

$$P' - E' = \underbrace{\beta(P - E)}_{\text{term 1}} - \underbrace{\frac{1}{2\pi a^2} F_L \frac{d\beta}{dx}}_{\text{term 2}}, \quad (18)$$

where

$$\beta = \left( \alpha - \frac{2}{T} \right) T' + \frac{dT'/dx}{dT/dx}. \quad (19)$$

Equation (18) implies that the pattern of  $P - E$  change is amplified under global warming by a factor of  $\beta(x)$ . Term 1 represents changes to the moisture content of the atmosphere, while term 2 represents changes to the poleward moisture transport by eddies. HS06 argue that Eq. (18) can be simplified to Eq. (4) by ignoring changes in the pattern of warming, which means that  $\beta$  is approximately uniform and thus term 2 in Eq. (18) is close to zero, making  $P' - E' \approx \beta(P - E) = \alpha T'(P - E)$ , or exactly Eq. (4). These arguments make sense for uniform warming, which indeed leads to term 2 in Eq. (18) being close to zero and the structure of  $P - E$  change is simply the existing pattern of  $P - E$  amplified by the pattern of warming, which is consistent with Fig. 7c. However, under polar-amplified warming these arguments make less sense, as strong meridional variations in  $T'$  act to alter both term 1 and term 2.

Figure 10 shows a decomposition of  $P' - E'$  for each pattern of  $\lambda$  in the Northern and Southern Hemisphere extratropics

(poleward of 30°) using the two terms in Eq. (18), the MEBM solution, and the HS06 approximation from Fig. 7. Under uniform warming, where the MEBM and HS06 approximation are approximately equal, the contribution of changes to the poleward moisture transport is relatively small (Fig. 10a). This occurs because  $dT'/dx = 0$ , making  $\beta$  relatively uniform and thus the transport of moisture [i.e., term 2 in Eq. (18)] is close to zero. However, under polar-amplified warming the MEBM and HS06 approximation diverge because of changes to spatial structure of  $\beta$  and changes to the poleward moisture transport (Figs. 10b–d). Because  $T'$  increases with latitude, the meridional temperature gradient weakens and therefore  $\beta$  decreases everywhere, which partially offsets the Clausius–Clapeyron effect. The same feature is seen under an asymmetric pattern of warming (Fig. 10d). When warming is amplified mainly in the Arctic, there is a reduction of  $P' - E'$  equal to approximately 0.2 mm day<sup>−1</sup> uniformly in the Northern Hemisphere extratropics. This decrease in poleward moisture transport reduces the enhancement of  $P' - E'$  in the high latitudes, and brings the MEBM in line with the changes seen in GCMs.

### d. Connection to CMIP5 hydrological changes

Armed with a better understanding of processes that set the pattern of  $P' - E'$  in the tropics and extratropics, we now revisit the ability of the MEBM to emulate comprehensive GCMs in CMIP5 using the same scalings from the previous sections.

#### 1) TROPICAL HYDROLOGICAL CHANGES

Figure 11 shows a decomposition of  $P' - E'$  associated with the three terms of Eq. (15), which detail thermodynamic and dynamic changes to  $P - E$  under warming. This is the same decomposition shown in Fig. 8, but for each individual GCM. Across most GCMs, changes to  $\psi$  are large and have a large impact on the  $P - E$  changes in the deep tropics. The change in  $\psi$  results in enhancement of  $P - E$  in the deep tropics. Between 5°S and 5°N, changes to  $\psi$  contribute to an enhancement of approximately 0.6 mm day<sup>−1</sup> in  $P - E$ . In GCMs with larger  $P - E$  changes in the deep tropics (e.g., ACCESS1.0 and MIROC-ESM),  $\nabla \cdot (\psi' L_v \bar{q})$  and  $\nabla \cdot (\psi' L_v q')$  contributes to 0.8–0.9 mm day<sup>−1</sup> in  $P - E$  changes. Conversely, in GCMs with smaller  $P - E$  changes in the deep tropics (e.g., CCSM4 and INM-CM4),  $\nabla \cdot (\psi' L_v \bar{q})$  and  $\nabla \cdot (\psi' L_v q')$  contributes 0.3–0.4 mm day<sup>−1</sup> in  $P - E$  changes. Additionally, GCMs with stronger hemispheric asymmetry in subtropical drying (e.g., GFDL-ESM2M, HadGEM2-ES) exhibit this asymmetry because of the dynamical terms (purple line).

Indeed,  $P - E$  change in the deep tropics is significantly impacted by changes in Hadley cell strength. The mechanism for this is detailed in Fig. 9 and related to the fact that some GCMs exhibit a narrowly peaked pattern of less negative or even positive feedback values in the deep tropics near the equator. This radiative feedback pattern implies more strengthening of  $\psi$  around the equator and less strengthening (or weakening) of  $\psi$  in the subtropics, thereby changing the spatial structure of  $\psi$ . In fact, the average radiative feedback value in the deep tropics (averaged between 5°S and 5°N) is strongly correlated ( $r = 0.68$ )

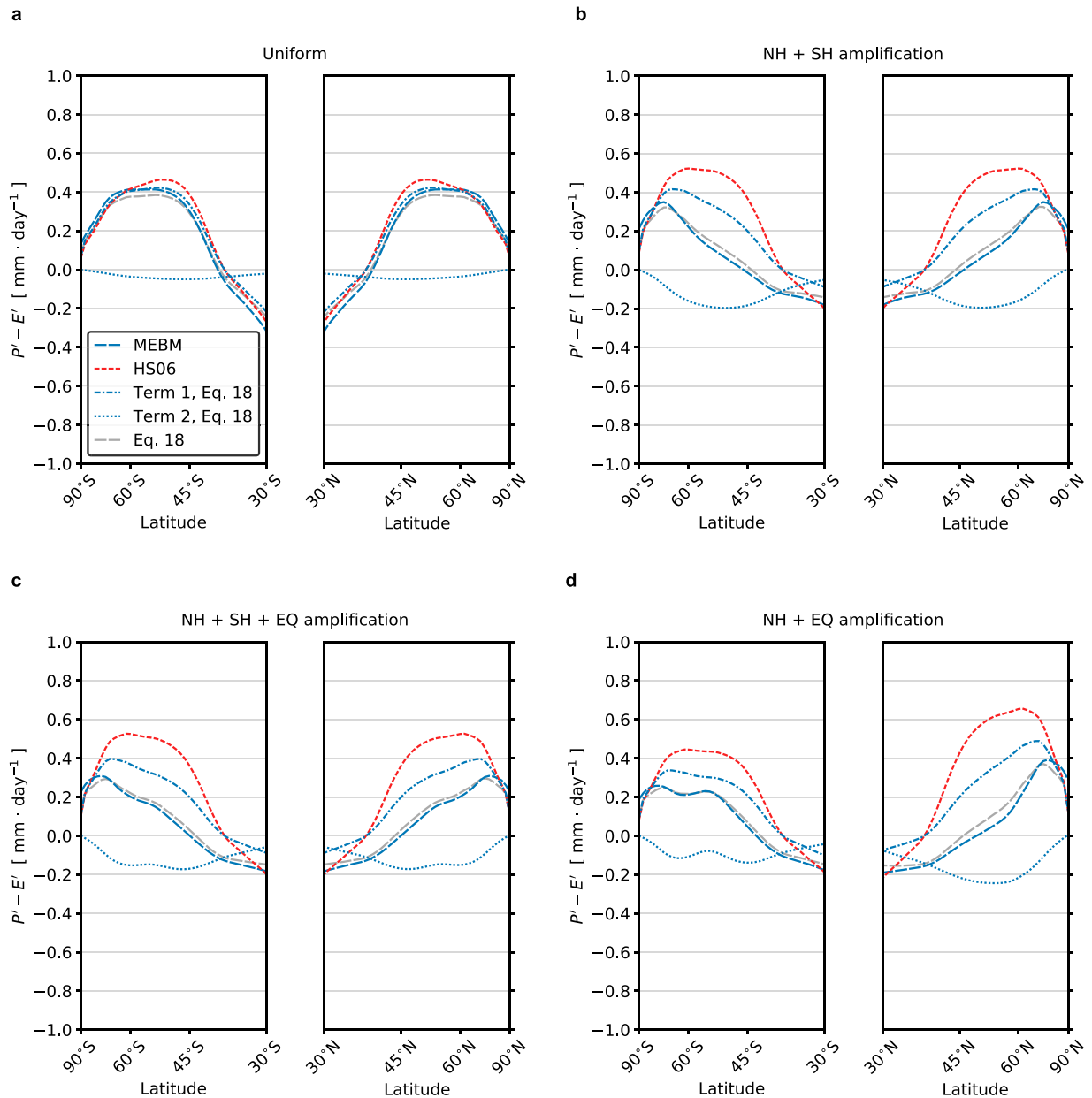


FIG. 10. Impact of radiative feedback patterns on the extratropical hydrological cycle response. The pattern of  $P' - E'$  poleward of  $30^{\circ}\text{S}$  and  $30^{\circ}\text{N}$  for a pattern of warming: (a) that is uniform, (b) with equal degrees of polar amplification in the Northern Hemisphere and Southern Hemisphere, (c) with equal degrees of polar amplification in the Northern Hemisphere and Southern Hemisphere and amplified warming on the equator, and (d) with more polar amplification in the Northern Hemisphere than Southern Hemisphere and amplified warming on the equator (see Fig. 7). These are found following section 4a (see Fig. 7). The blue dashed line denotes the MEBM solution. The red dashed line denotes the HS06 approximation assuming  $\alpha = 7\% \text{ K}^{-1}$  globally. The blue dash-dotted line is the  $P' - E'$  pattern from term one in Eq. (18), which represents changes to moisture content of the atmosphere with no changes to the transport of moisture. The blue dotted line is the  $P' - E'$  pattern from term two in Eq. (18), which represents changes to the transport of moisture under warming. The gray dashed line is the  $P' - E'$  pattern with transport changes included in addition to the full spatial structure of  $\beta$  [Eq. (18)].

with the  $P' - E'$  values between  $5^{\circ}\text{S}$  and  $5^{\circ}\text{N}$ . Similarly, the average divergence of the northward column-integrated atmosphere energy transport averaged between  $5^{\circ}\text{S}$  and  $5^{\circ}\text{N}$  is also strongly correlated ( $r = 0.72$ ) with the  $P' - E'$  values between  $5^{\circ}\text{S}$  and  $5^{\circ}\text{N}$ . This highlights the importance of radiative feedbacks in

setting poleward heat transport, which acts to strengthen the Hadley cell circulation in the deep tropics and enhance  $P - E$ .

The skill of the MEBM in emulating the Hadley cell mass flux changes is further compared with the actual streamfunction of the CMIP5 GCMs, which is calculated as

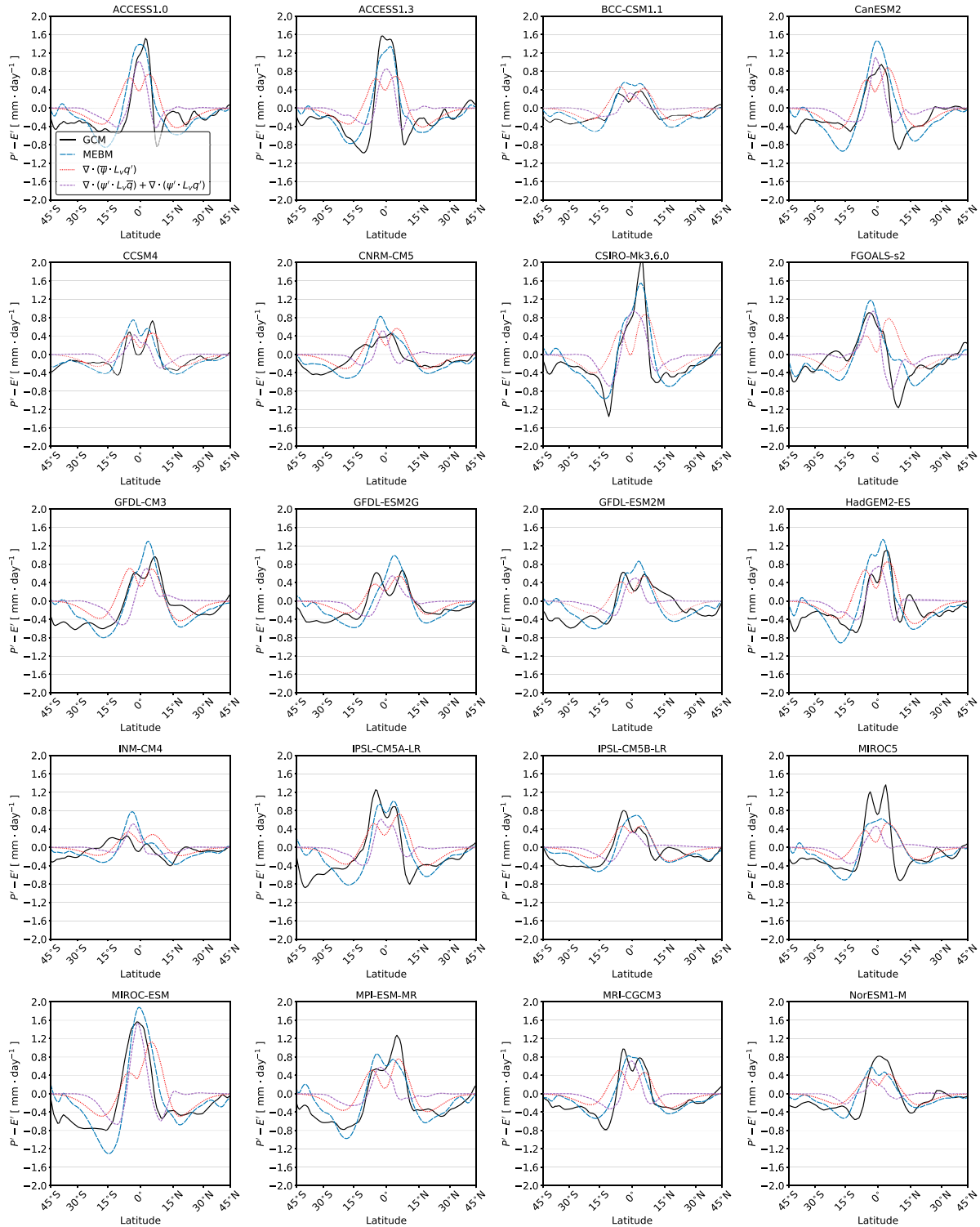


FIG. 11. Tropical hydrological changes in CMIP5. The pattern of  $P' - E'$  between  $45^{\circ}\text{S}$  and  $45^{\circ}\text{N}$  for each GCM. The black line denotes the GCM. The blue dashed line denotes the MEBM solution. The red dotted line is the  $P' - E'$  pattern from the MEBM with no circulation strength changes and changes to the moisture content of the atmosphere,  $\nabla \cdot (\bar{\psi} L_v q')$ . The purple dashed line is the  $P' - E'$  pattern from the MEBM with circulation strength changes and changes to the moisture content of the atmosphere,  $\nabla \cdot (\psi' L_v \bar{q}) + \nabla \cdot (\bar{\psi} L_v q')$ . Note that the latitude range is confined to  $45^{\circ}$  as this is where the Hadley cell parameterization begins to exhibit little-to-no influence on moisture transport.



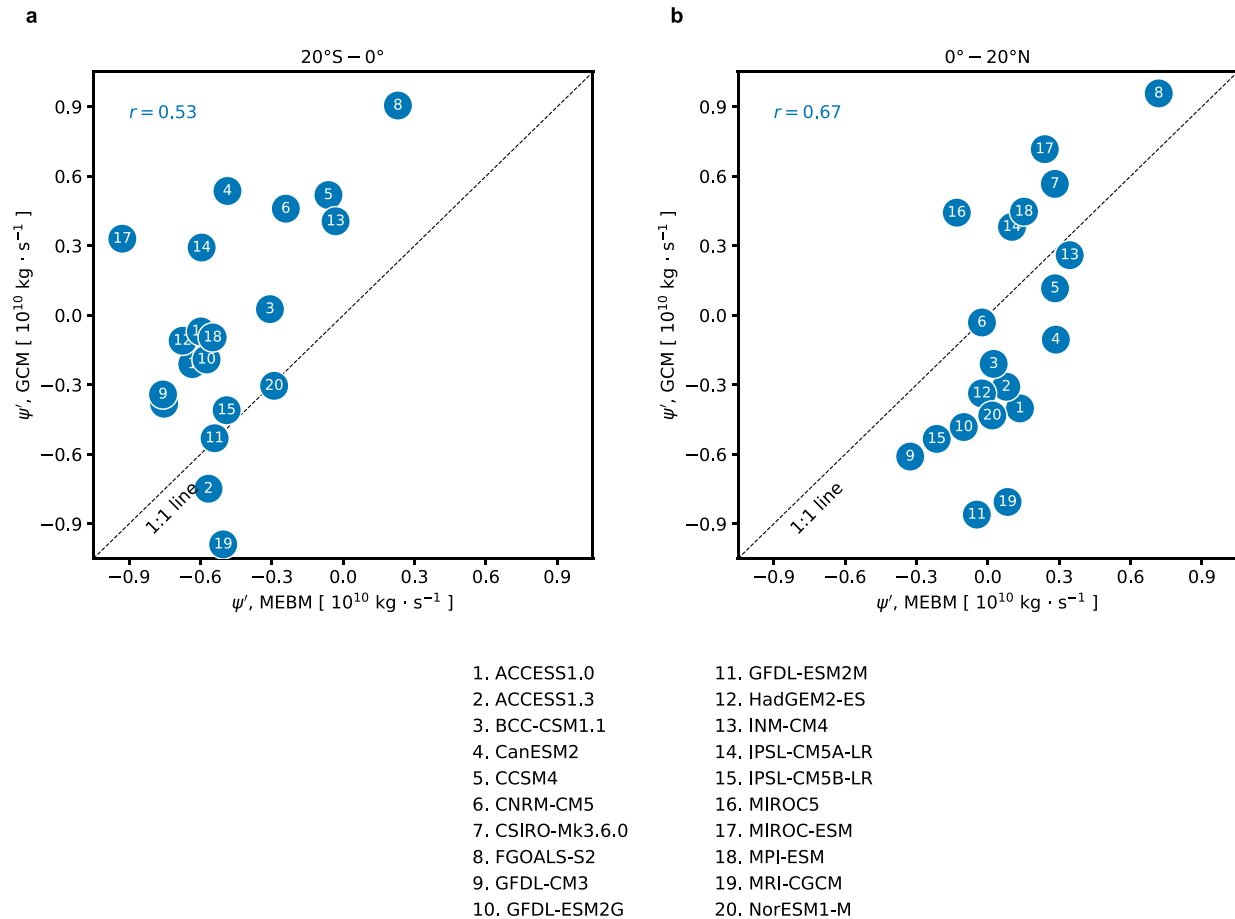


FIG. 12. Comparison of the Hadley cell mass-flux changes. Scatterplots of the area-averaged Hadley cell mass-flux change in each GCM and MEBM simulation for (a)  $20^{\circ}\text{S} - 0^{\circ}$  and (b)  $0^{\circ} - 20^{\circ}\text{N}$ . The top-left corner of the plot shows the Pearson correlation coefficient between MEBM and GCM.

$$\psi(x, p) = \frac{2\pi a}{g} \sqrt{(1-x^2)} \int_0^{p_s} [\bar{v}] dp, \quad (20)$$

where  $[\bar{v}]$  is zonal-mean and time-mean meridional velocity as a function of latitude and pressure  $p$ . To compare the Hadley cell mass flux of each GCM with the MEBM, we take the maximum magnitude (positive or negative) of the meridional mass streamfunction in Eq. (20) to produce the CMIP5 Hadley cell mass-flux strength  $\psi_{\text{max}}(x)$ .

The strengthening of the Hadley cell in the deep tropics and the weakening of the subtropics in the MEBM is consistent with the response from CMIP5 GCMs (not shown), but the MEBM tends to underpredict changes to  $\psi_{\text{max}}$  in each hemisphere, which can be seen in Fig. 12. However, the average mass-flux change of the MEBM in the deep tropics of the Southern Hemisphere ( $20^{\circ}\text{S} - 0^{\circ}$ ) and Northern Hemisphere ( $0^{\circ} - 20^{\circ}\text{N}$ ) is well correlated ( $r = 0.53$  and  $0.67$ ) with the Hadley cell mass-flux change in CMIP5 (Fig. 12). Further work is required to understand the precise reasons why the MEBM and the CMIP5 GCMs agree well and how these results connect to the dynamical theories of the Hadley cell circulation (Held and Hou 1980; Schneider 2006). Furthermore, it

is unclear here if the pattern of radiative feedbacks arises from the circulation changes and the MEBM simply captures this relationship. Nonetheless, the agreement suggests that downgradient energy transport provides a strong constraint on the Hadley cell mass-flux changes and tropical  $P - E$  changes.

## 2) EXTRATROPICAL HYDROLOGICAL CHANGES

Figure 13 shows a decomposition of  $P' - E'$  poleward of  $30^{\circ}$  into the two terms from Eq. (18), which represent changes to the moisture content of the atmosphere and changes to the poleward moisture flux. This is the same decomposition shown in Fig. 10, but for each individual GCM. Across all GCMs it is evident that reduced poleward moisture transport helps to align the MEBM with GCMs. The poleward moisture transport (i.e., term 2) decreases in both hemispheres across most GCMs and accounts for  $0.1 - 0.2 \text{ mm day}^{-1}$  decrease in  $P - E$ . The reduced poleward moisture transport also causes the expansion of the subtropics in each GCM, which is shown by the more poleward latitude of  $P - E = 0$ . While not shown in Fig. 13, GCMs with a stronger polar amplification tend to

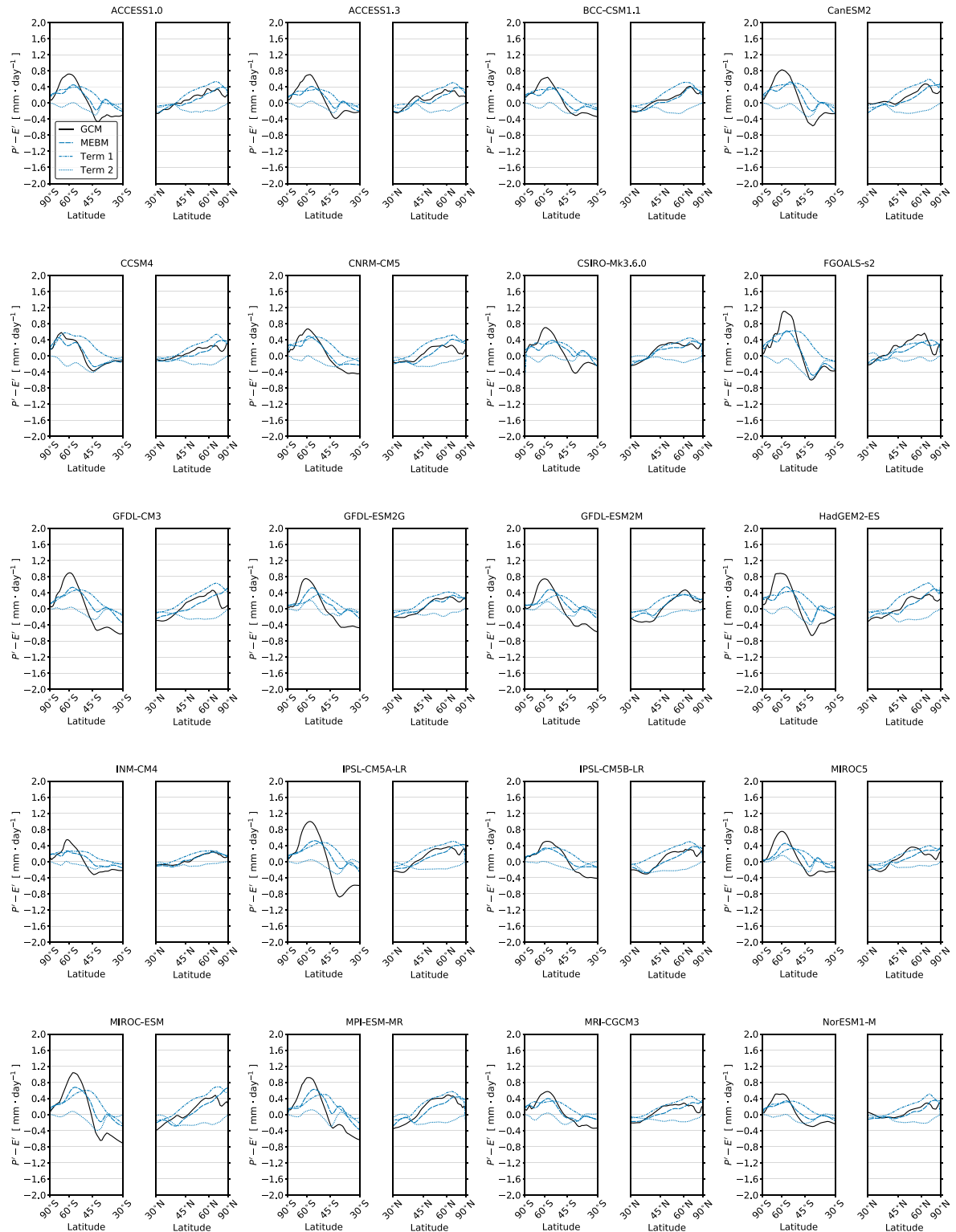


FIG. 13. Extratropical hydrological changes in CMIP5. The pattern of  $P' - E'$  poleward of  $30^\circ$ . The black line denotes the GCM response. The blue dashed line denotes the MEBM solution. The blue dash-dotted line is the  $P' - E'$  pattern from term one in Eq. (18) using MEBM output, which represents changes to moisture content of the atmosphere with no changes to the transport of moisture. The blue dotted line is the  $P' - E'$  pattern from term two in Eq. (18) using MEBM output, which represents changes to the transport of moisture under warming.

have a stronger reduction in the poleward moisture transport, and stronger subtropical drying.

## 5. Discussion and conclusions

Changes to  $P - E$  over the twenty-first century are predicted to impact ecosystems and socioeconomic activities throughout the world. While it is expected that, broadly, dry regions will get drier and wet regions will get wetter, the magnitude and spatial structure of  $P - E$  changes remains uncertain. In this paper, we examined the response of  $P - E$  to warming using a modified MEBM that reroutes moisture transport in the deep tropics with a Hadley Cell parameterization (Siler et al. 2018). We showed that the MEBM accurately emulates  $P - E$  change and accounts for a majority of the intermodel variance in  $P - E$  change as simulated by GCMs under greenhouse gas forcing. We then used the MEBM to identify sources of uncertainty in the pattern of  $P - E$  change under warming. Using zonal-mean patterns of radiative forcing  $R_f$ , ocean heat uptake  $G'$ , and the net radiative feedback  $\lambda$  from a suite of GCMs under  $4 \times \text{CO}_2$ , we showed that the MEBM accounts for the majority of the intermodel variance in  $P - E$  change in the deep tropics, subtropics, and extratropics. The intermodel spread in  $P - E$  change in these regions arises primarily from intermodel differences in  $\lambda$ , with  $R_f$  and  $G'$  playing secondary roles. However, in regions where regional ocean circulation shapes the rate of warming,  $G'$  can account for 30%–40% of the intermodel variance in  $P - E$  change. Finally, by confining the intermodel spread of  $\lambda$  to different regions, we showed that intermodel variations in tropical  $\lambda$  impact  $P - E$  change globally, whereas intermodel variations in polar  $\lambda$  mainly impact  $P - E$  change in the poles.

Motivated by the fact that  $\lambda$  plays a leading role in setting zonal-mean  $P - E$  change, we constructed a set of idealized  $\lambda$  patterns and used some extended scalings to further investigate the processes impacting zonal-mean  $P - E$  change. We demonstrated that  $P - E$  change depends crucially on the meridional pattern of warming and the anomalous net energy input into the atmosphere. Under uniform warming,  $P - E$  change occurs at approximately the Clausius–Clapeyron rate, consistent with the thermodynamic scaling first introduced by HS06. However, under polar-amplified warming, moisture transport to the high latitudes decreases, causing less of an increase in  $P - E$  in the high latitudes when compared to the HS06 approximation. Interestingly, when  $\lambda$  is less negative near the equator and begins to taper off in the subtropics,  $P - E$  in the deep tropics increases and the ITCZ region narrows, deviating strongly from the thermodynamic scaling of HS06. This occurs because the anomalous net energy input into the atmosphere cannot be radiated away locally at the equator, which means the Hadley cell mass flux  $\psi$  must strengthen in the deep tropics to transport that excess energy away. However, the concurrent increase in gross moist stability, which weakens  $\psi$ , outcompetes the poleward heat transport changes in the subtropics, where moist-static energy gradients are stronger. These two processes change the spatial structure of  $\psi$  and cause a convergence of moisture in the deep tropics, increasing  $P - E$  in the tropics and decreasing

$P - E$  in the subtropics. Of course, it is possible that the  $\lambda$  patterns themselves result from these circulation changes, and our results simply confirm the tightly coupled nature of hydrological changes and radiative response in the deep tropics. Still, our results demonstrate the importance for circulation changes and how radiative feedbacks relate to them. More work is required to understand whether the circulation responses give rise to the radiative feedbacks and the radiative feedbacks simply reflect these changes. Finally, under hemispherically asymmetric warming, where warming is more amplified in the Arctic when compared to the Antarctic, we find the subtropics dry less in the Northern Hemisphere when compared to the Southern Hemisphere. This mimics the hemispheric asymmetry of subtropical drying seen in GCMs and is traced to the asymmetric response of the changing atmospheric circulation. These circulation-strength changes can be understood as a consequence of the demands of overall downgradient energy transport, as encapsulated in the MEBM.

Our study has several implications. Given the role of polar amplification in setting the magnitude of the poleward moisture flux, the large spread in Arctic amplification among GCMs (Pithan and Mauritsen 2014; Bonan et al. 2018; Feldl et al. 2020) may also explain the large uncertainty in  $P - E$  changes, particularly for the Northern Hemisphere extratropics. Similarly, the relative warming of the Arctic versus the Antarctic, and the processes contributing to this asymmetry may explain intermodel differences in the amount of subtropical drying between each hemisphere by affecting the poleward heat flux, and thus the strength of the Hadley cell circulation. Furthermore, the role that radiative feedbacks play in setting  $P - E$  changes under warming suggests that studying the effect of each individual radiative feedback may help identify limits of the “wet-gets-wetter, dry-gets-drier” paradigm, and offer insights into potential biases in GCMs. Analysis of individual radiative feedbacks in the MEBM might also improve understanding of how feedbacks influence the circulation responses in so-called “feedback locking” experiments. Finally, our results indicate that changes to large-scale tropical circulations can be energetically constrained with a simple rule of downgradient energy transport, and that this rule helps to explain the narrowing of the ITCZ and hemispheric asymmetry in subtropical drying. Understanding how energetic constraints can be used to understand other dynamical features in GCMs (e.g., Feldl and Bordoni 2016) or the seasonality of  $P - E$  changes should be the subject of future work.

This study, however, contains a few caveats. In the MEBM the spatial patterns of  $R_f$ ,  $\lambda$ , and  $G'$  are prescribed and do not change over time. Thus, we are unable to consider transient  $P - E$  changes under global warming or the extent to which the spatial patterns of  $\lambda$  and  $G'$  are truly independent of atmospheric energy transport and the circulation responses themselves. Furthermore, the assumption that  $D$  is spatially uniform and invariant under warming is surely a crude approximation. Previous work has shown that  $D$  can be approximately 75% larger in the midlatitudes when compared to the subtropics (Frierson et al. 2007; Peterson and Boos 2020) and

can affect the degree of meridional shifts in tropical rainfall (Peterson and Boos 2020).  $D$  has also been shown to decrease under sustained greenhouse gas forcing (Shaw and Voigt 2016; Mooring and Shaw 2020). Future work might explore the impact of spatial patterns of  $D$ . Finally, the Hadley cell parameterization is limited as it does not account for changes between latent-energy transport accomplished by eddies and the Hadley cell under warming; or changes to the structure of upper-tropospheric moist-static energy under warming. For instance, the disagreement between subtropical  $P' - E'$  in MEBM and GCMs is likely related to the fact that the Hadley cell mass-flux change is small outside of the deep tropics and systematically underestimated in the MEBM. Future work might also explore the impact of allowing for the Hadley cell edge to change under warming (e.g., O’Gorman and Schneider 2008; Mbengue and Schneider 2018) or for better parameterizations of gross moist stability like making it proportional to the meridional gradient in moist static energy (e.g., Frierson et al. 2006; Frierson 2008) or dependent on the location of the ITCZ. Such work might help reconcile these results with the momentum-based theories of the Hadley cell (Held and Hou 1980; Schneider 2006).

Despite these shortcomings, the fact that the MEBM emulates zonal-mean  $P - E$  changes as simulated in GCMs under greenhouse gas forcing, suggests that the MEBM and the processes it represents offers a parsimonious understanding of the causes of hydrological change that is distinct from the simple thermodynamic scaling that results in the “wet-gets-wet, dry-gets-drier” paradigm. Specifically, in this paper, we showed how the MEBM captures changes to moisture transport in both the tropics and high latitudes that is not captured in other hydrological scalings. This work demonstrates that the spatial structure of radiative feedbacks can greatly impact changes to the strength of the Hadley cell circulation, acting to increase  $P - E$  in the deep tropics, decrease  $P - E$  in the subtropics, and narrow the ITCZ. This work also demonstrates the utility of downgradient energy transport to examine drivers of the intermodel spread in  $P - E$  changes. Our results suggest that, for as long as tropical feedbacks and polar amplification remain uncertain and poorly constrained among GCMs, projections of the spatial pattern of hydrological change will also remain uncertain. More broadly, our results imply that downgradient energy transport and energetic constraints on the strength of the Hadley cell circulation provide an alternative and perhaps more fundamental explanation for the response of  $P - E$  to climate change.

*Acknowledgments.* The authors thank Polina Khapikova for helpful comments on an earlier draft of this paper. The authors also thank three reviewers and the editor for helpful and encouraging comments. Part of this research was supported by the University of Washington Mary Gates Endowment for Undergraduate Students. D.B.B was supported by an American Meteorological Society (AMS) Graduate Fellowship and the National Science Foundation (NSF) Graduate Research Fellowship Program (NSF Grant DGE1745301). N.S. was supported by NSF Grant AGS-1954663. G.H.R. was

supported by NSF Grants AGS-2019647 and P2C2-2102829. K.C.A. was supported by NSF Grants AGS-1752796 and AGS-2019647, and an Alfred P. Sloan Research Fellowship (Grant FG-2020-13568). We thank the climate modeling groups for producing and making available their model output, which is accessible at the Earth System Grid Federation (ESGF) Portal (<https://esgf-node.llnl.gov/search/cmip5/>).

*Data availability statement.* The code and data for this study are available at <https://github.com/dbonan/energy-balance-models>.

## APPENDIX A

### CMIP5 Output

We use monthly output from 20 different GCMs participating in phase 5 of the Coupled Model Intercomparison Project (CMIP5; Taylor et al. 2012). This subset of GCMs reflects those that provide the necessary output for calculating  $R_f(x)$ ,  $G'(x)$ , and  $\lambda(x)$ . For each GCM, we calculate anomalies in each variable, denoted by prime, as the difference between the variable averaged over a preindustrial control simulation and the variable averaged over the last 25 years of  $4 \times \text{CO}_2$  simulations (years 126–150). All variables are annual and zonal means computed from monthly output. The variables include all-sky shortwave and longwave radiation at the surface and top-of-the-atmosphere (rsds, rsus, rsdt, rsut, rlds, rlus, rlut), sensible and latent heat fluxes (hfss, hfls), sea surface temperature (tos), near-surface air temperature (tas), precipitation (pr), and evaporation (evs).

The  $R_f(x)$  is calculated from the change in top of atmosphere (TOA) radiation in  $4 \times \text{CO}_2$  simulations performed with fixed preindustrial sea surface temperatures (Siler et al. 2019). The  $G'(x)$  is calculated as the change in net surface heat fluxes in  $4 \times \text{CO}_2$  simulations performed in fully coupled GCMs. The  $\lambda(x)$  is calculated by equating the zonal-mean net TOA radiation anomaly with  $\lambda(x)T'(x) + R_f(x)$ . Figure A1 shows the patterns of  $R_f(x)$ ,  $G'(x)$ , and  $\lambda(x)$  for each GCM.

## APPENDIX B

### Climatological Hadley Cell Parameterization

In the main text, we introduce the Hadley cell parameterization using the perturbation version of the MEBM. However, the mass transport of the Hadley cell and thus the pattern of  $P' - E'$  depends to some extent on the climatological state via Eqs. (10) and (11). To account for this, we use a climatological version of the MEBM to estimate the climatological state of each GCM. This is done by first calculating the net heating of the atmosphere  $Q_{\text{net}}(x)$ , which is the difference between the net downward energy flux at the TOA and the surface in preindustrial control simulations (see appendix A). Because the northward column-integrated atmospheric energy transport  $F$  is assumed to be related to

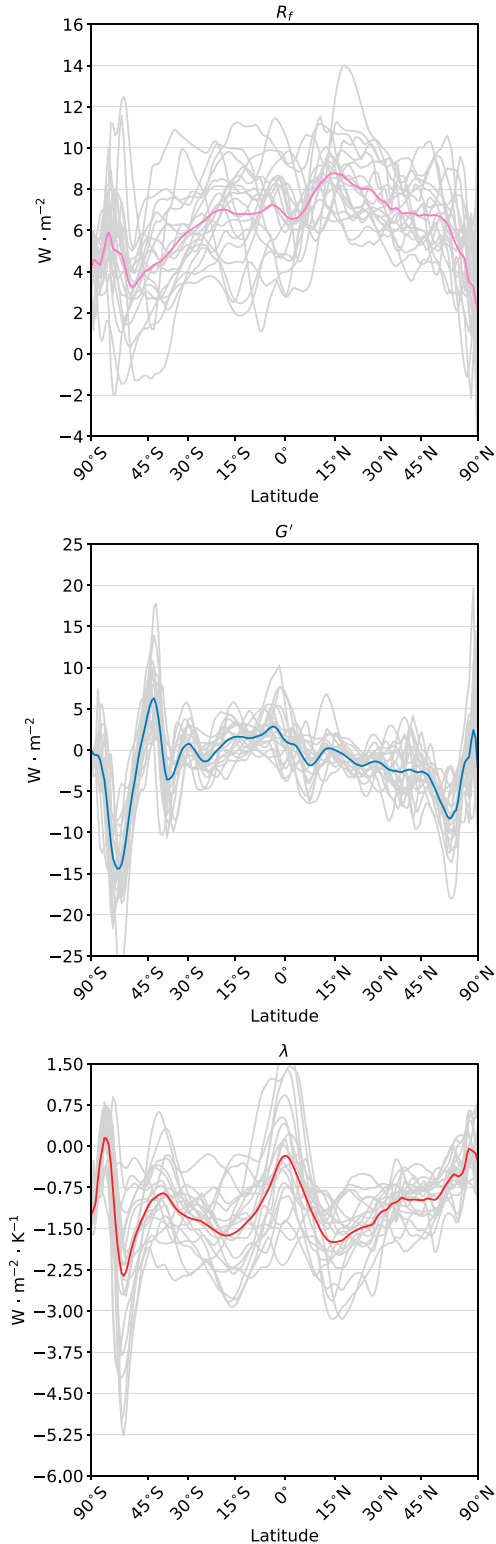


FIG. A1. Input to the moist energy balance model. The zonal-mean profile of (a) radiative forcing ( $R_f$ ), (b) ocean heat uptake ( $G'$ ), and (c) the net radiative feedback ( $\lambda$ ) from 20 CMIP5 GCMs 126–150 years after an abrupt quadrupling of  $\text{CO}_2$ . The gray lines represent each individual GCM, and the colored lines denote the multimodel mean.

the meridional gradient in  $h$ , the climatological version of the MEBM (with a constant  $D$ ) is

$$Q_{\text{net}}(x) = -\frac{P_s}{a^2 g} D \frac{d}{dx} \left[ (1 - x^2) \frac{dh}{dx} \right]. \quad (\text{B1})$$

The MEBM climatological values of  $T(x)$  and  $q(x)$  (assuming relative humidity is fixed at 80%) can be found by minimizing the difference between the zonal-mean near-surface air temperature and  $Q_{\text{net}}$  from each GCM using Eq. (B1). A similar procedure as described in section 2 is then used to calculate  $\psi(x)$ ,  $H(x)$ , and  $P - E$  except that the poleward heat flux and moisture flux take the form of

$$F_{\text{HC}}(x) = \psi(x)H(x), \quad \text{and} \quad (\text{B2})$$

$$F_{L,\text{HC}}(x) = -\psi(x)L_v q(x), \quad (\text{B3})$$

respectively. Note that here  $D$  is unique to each GCM. For section 3, the value of  $D$  is unique to each GCM and for section 4, the value of  $D$  is  $1.05 \times 10^6 \text{ m}^2 \text{ s}^{-1}$  (i.e., the multimodel mean value). For section 3, the climatological variables are unique to each GCM and for section 4, the climatological variables are the multimodel mean patterns and made to be symmetric about the equator.

## APPENDIX C

### Diffusive Energy Transport Scaling

The scaling in Eq. (18) was first derived by HS06 and can be found through the following arguments. First, by assuming that moisture and temperature are diffused with the same diffusivity, the ratio of the latent heat transport  $F_L$  to the sensible heat transport  $F_S$  will be the ratio of the meridional gradient of  $L_v q$  to the meridional gradient of  $c_p T$ , meaning:

$$\frac{F_L}{F_S} = \frac{L_v dq}{c_p dT}, \quad (\text{C1})$$

where

$$\frac{dq}{dT} = \frac{dq/dx}{dT/dx}. \quad (\text{C2})$$

Because the Clausius–Clapeyron equation states that

$$\frac{dq}{dT} = \alpha q, \quad (\text{C3})$$

the fractional change in the moisture transport under warming can be approximated as

$$\frac{F'_L}{F_L} \approx \frac{(\alpha q)'}{\alpha q} + \frac{F'_S}{F_S}, \quad (\text{C4})$$

which can be rearranged to be

$$\frac{F'_L}{F_L} \approx \left( \alpha - \frac{2}{T} \right) T' + \frac{F'_S}{F_S}. \quad (\text{C5})$$

Thus, the change in moisture transport under warming can be written as

$$F'_L(x) \approx \beta F_L(x), \quad (\text{C6})$$

where

$$\beta = \left( \alpha - \frac{2}{T} \right) T' + \frac{dT'/dx}{dT/dx}. \quad (\text{C7})$$

Note that the fractional change in sensible heat transport is now written in terms of the gradient in near-surface air temperature. Finally, the change in  $P - E$  under warming can be found by taking the divergence of Eq. (C6) which, together with Eq. (C7), results in

$$P' - E' = \underbrace{\beta(P - E)}_{\text{term 1}} - \underbrace{\frac{1}{2\pi a^2} F_L \frac{d\beta}{dx}}_{\text{term 2}}. \quad (\text{C8})$$

Here, term 1 represents changes to the moisture content of the atmosphere under warming and term 2 represents changes to the poleward moisture flux under warming. HS06 argue that the dependence of the saturation vapor pressure on  $T$  and the fractional change of sensible-heat transport in Eq. (C7) are small and can be ignored. They also argue that because the pattern of warming is relatively uniform, the second term on the right-hand side of Eq. (C8), which represents changes to the transport of moisture, is close to zero. Removing these terms results in  $P' - E' = \beta(P - E) = \alpha T'(P - E)$ , which is exactly Eq. (4). Thus, for the extratropics, the HS06 scaling and the MEBM differ because of the pattern of temperature change  $T'$  and the climatological pattern of  $T$ , which determine the moisture content of the atmosphere and poleward moisture transport.

## REFERENCES

- Abernathey, R. P., I. Cerovecki, P. R. Holland, E. Newsom, M. Mazloff, and L. D. Talley, 2016: Water-mass transformation by sea ice in the upper branch of the Southern Ocean overturning. *Nat. Geosci.*, **9**, 596–601, <https://doi.org/10.1038/ngeo2749>.
- Armour, K. C., N. Siler, A. Donohoe, and G. H. Roe, 2019: Meridional atmospheric heat transport constrained by energetics and mediated by large-scale diffusion. *J. Climate*, **32**, 3655–3680, <https://doi.org/10.1175/JCLI-D-18-0563.1>.
- Beer, E., and I. Eisenman, 2022: Revisiting the role of the water vapor and lapse rate feedbacks in the Arctic amplification of climate change. *J. Climate*, **35**, 2975–2988, <https://doi.org/10.1175/JCLI-D-21-0814.1>.
- Bonan, D. B., K. C. Armour, G. H. Roe, N. Siler, and N. Feldl, 2018: Sources of uncertainty in the meridional pattern of climate change. *Geophys. Res. Lett.*, **45**, 9131–9140, <https://doi.org/10.1029/2018GL079429>.
- Boos, W. R., 2012: Thermodynamic scaling of the hydrological cycle of the last glacial maximum. *J. Climate*, **25**, 992–1006, <https://doi.org/10.1175/JCLI-D-11-00010.1>.
- Burls, N. J., and A. V. Fedorov, 2017: Wetter subtropics in a warmer world: Contrasting past and future hydrological cycles. *Proc. Natl. Acad. Sci. USA*, **114**, 12 888–12 893, <https://doi.org/10.1073/pnas.1703421114>.
- Byrne, M. P., and P. A. O’Gorman, 2015: The response of precipitation minus evapotranspiration to climate warming: Why the “wet-get-wetter, dry-get-drier” scaling does not hold over land. *J. Climate*, **28**, 8078–8092, <https://doi.org/10.1175/JCLI-D-15-0369.1>.
- , and T. Schneider, 2016a: Energetic constraints on the width of the intertropical convergence zone. *J. Climate*, **29**, 4709–4721, <https://doi.org/10.1175/JCLI-D-15-0767.1>.
- , and —, 2016b: Narrowing of the ITCZ in a warming climate: Physical mechanisms. *Geophys. Res. Lett.*, **43**, 11 350–11 357, <https://doi.org/10.1002/2016GL070396>.
- Carmichael, M. J., and Coauthors, 2016: A model–model and data–model comparison for the early Eocene hydrological cycle. *Climate Past*, **12**, 455–481, <https://doi.org/10.5194/cp-12-455-2016>.
- Chadwick, R., I. Boutle, and G. Martin, 2013: Spatial patterns of precipitation change in CMIP5: Why the rich do not get richer in the tropics. *J. Climate*, **26**, 3803–3822, <https://doi.org/10.1175/JCLI-D-12-00543.1>.
- Chang, E. K. M., Y. Guo, and X. Xia, 2012: CMIP5 multimodel ensemble projection of storm track change under global warming. *J. Geophys. Res.*, **117**, D23118, <https://doi.org/10.1029/2012JD018578>.
- Chou, C., and J. D. Neelin, 2004: Mechanisms of global warming impacts on regional tropical precipitation. *J. Climate*, **17**, 2688–2701, [https://doi.org/10.1175/1520-0442\(2004\)017<2688:MOGWIO>2.0.CO;2](https://doi.org/10.1175/1520-0442(2004)017<2688:MOGWIO>2.0.CO;2).
- , —, C.-A. Chen, and J.-Y. Tu, 2009: Evaluating the “rich-get-richer” mechanism in tropical precipitation change under global warming. *J. Climate*, **22**, 1982–2005, <https://doi.org/10.1175/2008JCLI2471.1>.
- , T.-C. Wu, and P.-H. Tan, 2013: Changes in gross moist stability in the tropics under global warming. *Climate Dyn.*, **41**, 2481–2496, <https://doi.org/10.1007/s00382-013-1703-2>.
- Dai, A., and K. E. Trenberth, 2002: Estimates of freshwater discharge from continents: Latitudinal and seasonal variations. *J. Hydrometeorol.*, **3**, 660–687, [https://doi.org/10.1175/1525-7541\(2002\)003<0660:EOFDFO>2.0.CO;2](https://doi.org/10.1175/1525-7541(2002)003<0660:EOFDFO>2.0.CO;2).
- de Boyer Montégut, C., J. Mignot, A. Lazar, and S. Cravatte, 2007: Control of salinity on the mixed layer depth in the world ocean: 1. General description. *J. Geophys. Res.*, **112**, C06011, <https://doi.org/10.1029/2006JC003953>.
- Emori, S., and S. J. Brown, 2005: Dynamic and thermodynamic changes in mean and extreme precipitation under changed climate. *Geophys. Res. Lett.*, **32**, L17706, <https://doi.org/10.1029/2005GL023272>.
- Feldl, N., and S. Bordoni, 2016: Characterizing the Hadley circulation response through regional climate feedbacks. *J. Climate*, **29**, 613–622, <https://doi.org/10.1175/JCLI-D-15-0424.1>.
- , S. Po-Chedley, H. K. Singh, S. Hay, and P. J. Kushner, 2020: Sea ice and atmospheric circulation shape the high-latitude lapse rate feedback. *npj Climate Atmos. Sci.*, **3**, 41, <https://doi.org/10.1038/s41612-020-00146-7>.
- Field, C. B., and V. R. Barros, 2014: *Climate Change 2014—Impacts, Adaptation and Vulnerability: Regional Aspects*. Cambridge University Press, 696 pp.
- Flannery, B. P., 1984: Energy balance models incorporating transport of thermal and latent energy. *J. Atmos. Sci.*, **41**, 414–421, [https://doi.org/10.1175/1520-0469\(1984\)041<0414:EBMITO>2.0.CO;2](https://doi.org/10.1175/1520-0469(1984)041<0414:EBMITO>2.0.CO;2).

- Frierson, D. M. W., 2008: Midlatitude static stability in simple and comprehensive general circulation models. *J. Atmos. Sci.*, **65**, 1049–1062, <https://doi.org/10.1175/2007JAS2373.1>.
- , I. M. Held, and P. Zurita-Gotor, 2006: A gray-radiation aquaplanet moist GCM. Part I: Static stability and eddy scale. *J. Atmos. Sci.*, **63**, 2548–2566, <https://doi.org/10.1175/JAS3753.1>.
- , —, and —, 2007: A gray-radiation aquaplanet moist GCM. Part II: Energy transports in altered climates. *J. Atmos. Sci.*, **64**, 1680–1693, <https://doi.org/10.1175/JAS3913.1>.
- Groeskamp, S., S. M. Griffies, D. Iudicone, R. Marsh, A. J. G. Nurser, and J. D. Zika, 2019: The water mass transformation framework for ocean physics and biogeochemistry. *Annu. Rev. Mar. Sci.*, **11**, 271–305, <https://doi.org/10.1146/annurev-marine-010318-095421>.
- Held, I. M., 2001: The partitioning of the poleward energy transport between the tropical ocean and atmosphere. *J. Atmos. Sci.*, **58**, 943–948, [https://doi.org/10.1175/1520-0469\(2001\)058<0943:TPOTPE>2.0.CO;2](https://doi.org/10.1175/1520-0469(2001)058<0943:TPOTPE>2.0.CO;2).
- , and A. Y. Hou, 1980: Nonlinear axially symmetric circulations in a nearly inviscid atmosphere. *J. Atmos. Sci.*, **37**, 515–533, [https://doi.org/10.1175/1520-0469\(1980\)037<0515:NASCIA>2.0.CO;2](https://doi.org/10.1175/1520-0469(1980)037<0515:NASCIA>2.0.CO;2).
- , and B. J. Soden, 2006: Robust responses of the hydrological cycle to global warming. *J. Climate*, **19**, 5686–5699, <https://doi.org/10.1175/JCLI3990.1>.
- Hill, S. A., N. J. Burls, A. Fedorov, and T. M. Merlis, 2022: Symmetric and antisymmetric components of polar-amplified warming. *J. Climate*, **35**, 3157–3172, <https://doi.org/10.1175/JCLI-D-20-0972.1>.
- Hwang, Y.-T., and D. M. W. Frierson, 2010: Increasing atmospheric poleward energy transport with global warming. *Geophys. Res. Lett.*, **37**, L24807, <https://doi.org/10.1029/2010GL045440>.
- Kang, S. M., and J. Lu, 2012: Expansion of the Hadley cell under global warming: Winter versus summer. *J. Climate*, **25**, 8387–8393, <https://doi.org/10.1175/JCLI-D-12-00323.1>.
- Large, W. G., and A. G. Nurser, 2001: Ocean surface water mass transformation. *Ocean Circulation and Climate*, G. Siedler, J. Church, and J. Gould, Eds., International Geophysics Series, Vol. 77, Elsevier, 317–336.
- Lau, W. K. M., and K.-M. Kim, 2015: Robust Hadley circulation changes and increasing global dryness due to CO<sub>2</sub> warming from CMIP5 model projections. *Proc. Natl. Acad. Sci. USA*, **112**, 3630–3635, <https://doi.org/10.1073/pnas.1418682112>.
- Liu, M., G. Vecchi, B. Soden, W. Yang, and B. Zhang, 2021: Enhanced hydrological cycle increases ocean heat uptake and moderates transient climate change. *Nat. Climate Change*, **11**, 848–853, <https://doi.org/10.1038/s41558-021-01152-0>.
- Lu, J., G. A. Vecchi, and T. Reichler, 2007: Expansion of the Hadley cell under global warming. *Geophys. Res. Lett.*, **34**, L06805, <https://doi.org/10.1029/2006GL028443>.
- , G. Chen, and D. M. Frierson, 2010: The position of the mid-latitude storm track and eddy-driven westerlies in aquaplanet AGCMs. *J. Atmos. Sci.*, **67**, 3984–4000, <https://doi.org/10.1175/2010JAS3477.1>.
- Lutsko, N. J., J. T. Seeley, and D. W. Keith, 2020: Estimating impacts and trade-offs in solar geoengineering scenarios with a moist energy balance model. *Geophys. Res. Lett.*, **47**, e2020GL087290, <https://doi.org/10.1029/2020GL087290>.
- Marshall, J., J. R. Scott, K. C. Armour, J.-M. Campin, M. Kelley, and A. Romanou, 2015: The ocean's role in the transient response of climate to abrupt greenhouse gas forcing. *Climate Dyn.*, **44**, 2287–2299, <https://doi.org/10.1007/s00382-014-2308-0>.
- Mbengue, C., and T. Schneider, 2013: Storm track shifts under climate change: What can be learned from large-scale dry dynamics. *J. Climate*, **26**, 9923–9930, <https://doi.org/10.1175/JCLI-D-13-00404.1>.
- , and —, 2017: Storm-track shifts under climate change: Toward a mechanistic understanding using baroclinic mean available potential energy. *J. Atmos. Sci.*, **74**, 93–110, <https://doi.org/10.1175/JAS-D-15-0267.1>.
- , and —, 2018: Linking Hadley circulation and storm tracks in a conceptual model of the atmospheric energy balance. *J. Atmos. Sci.*, **75**, 841–856, <https://doi.org/10.1175/JAS-D-17-0098.1>.
- Merlis, T. M., and M. Henry, 2018: Simple estimates of polar amplification in moist diffusive energy balance models. *J. Climate*, **31**, 5811–5824, <https://doi.org/10.1175/JCLI-D-17-0578.1>.
- , T. Schneider, S. Bordoni, and I. Eisenman, 2013: Hadley circulation response to orbital precession. Part I: Aquaplanets. *J. Climate*, **26**, 740–753, <https://doi.org/10.1175/JCLI-D-11-00716.1>.
- Mitchell, J., C. Wilson, and W. Cunnington, 1987: On CO<sub>2</sub> climate sensitivity and model dependence of results. *Quart. J. Roy. Meteor. Soc.*, **113**, 293–322, <https://doi.org/10.1256/smsqj.47516>.
- Mooring, T. A., and T. A. Shaw, 2020: Atmospheric diffusivity: A new energetic framework for understanding the midlatitude circulation response to climate change. *J. Geophys. Res. Atmos.*, **125**, e2019JD031206, <https://doi.org/10.1029/2019JD031206>.
- O’Gorman, P. A., and T. Schneider, 2008: The hydrological cycle over a wide range of climates simulated with an idealized GCM. *J. Climate*, **21**, 3815–3832, <https://doi.org/10.1175/2007JCLI2065.1>.
- Peterson, H. G., and W. R. Boos, 2020: Feedbacks and eddy diffusivity in an energy balance model of tropical rainfall shifts. *npj Climate Atmos. Sci.*, **3**, 11, <https://doi.org/10.1038/s41612-020-0114-4>.
- Pithan, F., and T. Mauritsen, 2014: Arctic amplification dominated by temperature feedbacks in contemporary climate models. *Nat. Geosci.*, **7**, 181–184, <https://doi.org/10.1038/ngeo2071>.
- Prein, A. F., and A. G. Pendergrass, 2019: Can we constrain uncertainty in hydrologic cycle projections? *Geophys. Res. Lett.*, **46**, 3911–3916, <https://doi.org/10.1029/2018GL081529>.
- Raymond, D. J., S. L. Sessions, A. H. Sobel, and Ž. Fuchs, 2009: The mechanics of gross moist stability. *J. Adv. Model. Earth Syst.*, **1** (3), <https://doi.org/10.3894/JAMES.2009.1.9>.
- Roe, G. H., N. Feldl, K. C. Armour, Y.-T. Hwang, and D. M. Frierson, 2015: The remote impacts of climate feedbacks on regional climate predictability. *Nat. Geosci.*, **8**, 135–139, <https://doi.org/10.1038/ngeo2346>.
- Rusotto, R. D., and M. Biasutti, 2020: Polar amplification as an inherent response of a circulating atmosphere: Results from the TRACMIP aquaplanets. *Geophys. Res. Lett.*, **47**, e2019GL086771, <https://doi.org/10.1029/2019GL086771>.
- Scheff, J., and D. Frierson, 2012: Twenty-first-century multimodel subtropical precipitation declines are mostly midlatitude shifts. *J. Climate*, **25**, 4330–4347, <https://doi.org/10.1175/JCLI-D-11-00393.1>.
- Schmitt, R. W., P. S. Bogden, and C. E. Dorman, 1989: Evaporation minus precipitation and density fluxes for the North Atlantic. *J. Phys. Oceanogr.*, **19**, 1208–1221, [https://doi.org/10.1175/1520-0485\(1989\)019<1208:EMPADE>2.0.CO;2](https://doi.org/10.1175/1520-0485(1989)019<1208:EMPADE>2.0.CO;2).
- Schneider, T., 2006: The general circulation of the atmosphere. *Annu. Rev. Earth Planet. Sci.*, **34**, 655–688, <https://doi.org/10.1146/annurev.earth.34.031405.125144>.

- Seager, R., and G. A. Vecchi, 2010: Greenhouse warming and the 21st century hydroclimate of southwestern North America. *Proc. Natl. Acad. Sci. USA*, **107**, 21 277–21 282, <https://doi.org/10.1073/pnas.0910856107>.
- , N. Naik, and G. A. Vecchi, 2010: Thermodynamic and dynamic mechanisms for large-scale changes in the hydrological cycle in response to global warming. *J. Climate*, **23**, 4651–4668, <https://doi.org/10.1175/2010JCLI3655.1>.
- Shaw, T. A., and A. Voigt, 2016: What can moist thermodynamics tell us about circulation shifts in response to uniform warming? *Geophys. Res. Lett.*, **43**, 4566–4575, <https://doi.org/10.1002/2016GL068712>.
- Siler, N., G. H. Roe, and K. C. Armour, 2018: Insights into the zonal-mean response of the hydrologic cycle to global warming from a diffusive energy balance model. *J. Climate*, **31**, 7481–7493, <https://doi.org/10.1175/JCLI-D-18-0081.1>.
- , —, —, and N. Feldl, 2019: Revisiting the surface-energy-flux perspective on the sensitivity of global precipitation to climate change. *Climate Dyn.*, **52**, 3983–3995, <https://doi.org/10.1007/s00382-018-4359-0>.
- Su, H., J. H. Jiang, C. Zhai, T. J. Shen, J. D. Neelin, G. L. Stephens, and Y. L. Yung, 2014: Weakening and strengthening structures in the Hadley circulation change under global warming and implications for cloud response and climate sensitivity. *J. Geophys. Res. Atmos.*, **119**, 5787–5805, <https://doi.org/10.1002/2014JD021642>.
- , C. Zhai, J. H. Jiang, L. Wu, J. D. Neelin, and Y. L. Yung, 2019: A dichotomy between model responses of tropical ascent and descent to surface warming. *npj Climate Atmos. Sci.*, **2**, 8, <https://doi.org/10.1038/s41612-019-0066-8>.
- Taylor, K. E., R. J. Stouffer, and G. A. Meehl, 2012: An overview of CMIP5 and the experiment design. *Bull. Amer. Meteor. Soc.*, **93**, 485–498, <https://doi.org/10.1175/BAMS-D-11-00094.1>.
- Winguth, A., C. Shellito, C. Shields, and C. Winguth, 2010: Climate response at the Paleocene–Eocene Thermal Maximum to greenhouse gas forcing—A model study with CCSM3. *J. Climate*, **23**, 2562–2584, <https://doi.org/10.1175/2009JCLI3113.1>.